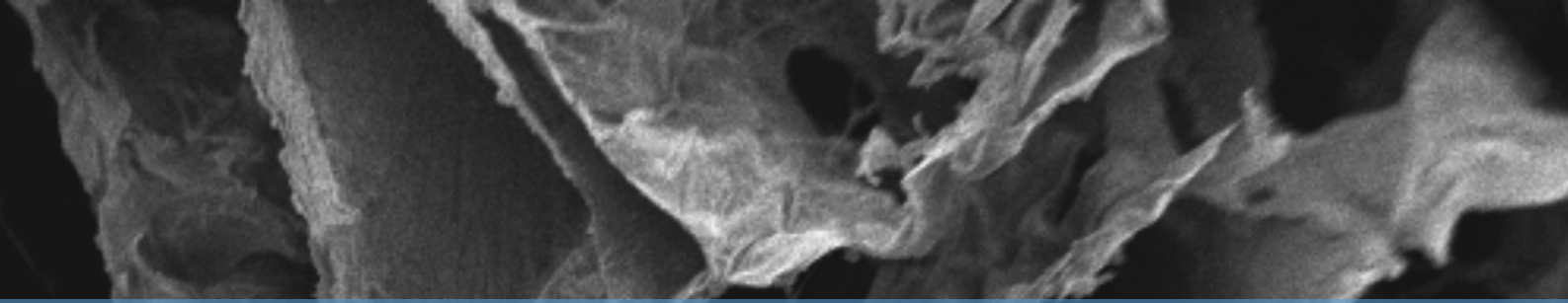

Development of a Two-Phase Scaffold-Nanoparticle System for the Sustained Delivery of Growth Factors in Bone Tissue Engineering Applications

Master's Thesis

by **Tinke-Marie De Witte**

June 22, 2018

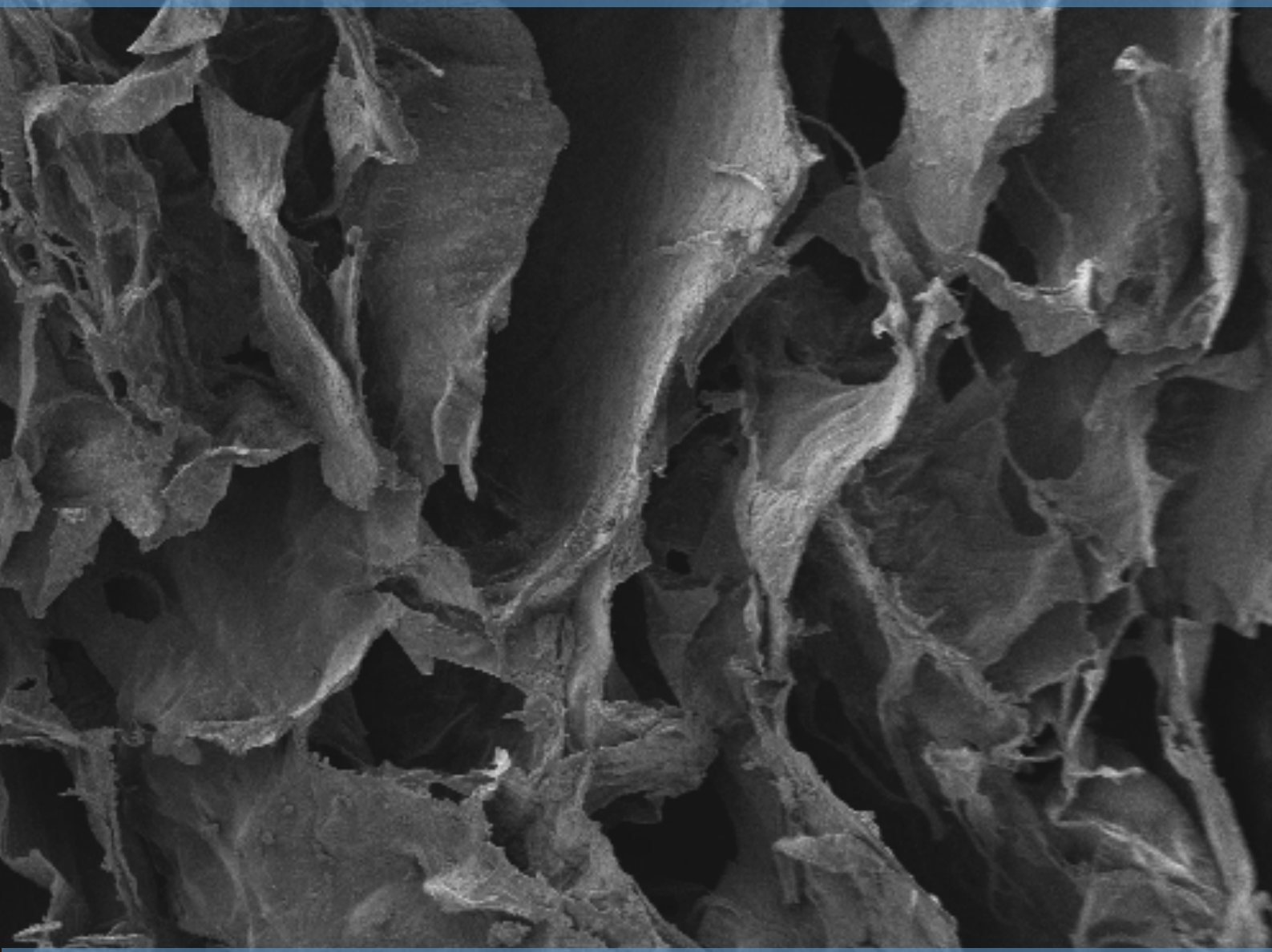

Supervisors:
Prof.dr. Nicholas A. Peppas
Assist.Prof.dr.ir. Lidy Fratila-Apachitei
Prof.dr. Amir Zadpoor

TEXAS
The University of Texas at Austin

TU Delft

Development of a Two-Phase Scaffold-Nanoparticle System for the Sustained Delivery of Growth Factors in Bone Tissue Engineering Applications

by

Tinke-Marie De Witte

in partial fulfillment of the requirements for the degree of

Master of Science
in Biomedical Engineering

at the Delft University of Technology,
to be defended publicly June 2018

Student Number	4628810	
Supervisors:	Prof.dr. Nicholas A Peppas	University of Texas at Austin
	Assist.Prof.dr.ir. Lidy Fratila-Apachitei	TU Delft
	Prof.dr. Amir Zadpoor	TU Delft

Acknowledgements

I would like to take the time to express my gratitude to those without whom this graduation research project would not have been possible. First, I would like to thank my supervisor, Nicholas Peppas, for giving me the unique opportunity to join his laboratory. I would like to thank you for taking a chance on me and making me feel like an integral member of your research team from the very first day. It has been an honor to join your lab and to bear witness to your breadth of knowledge and expertise. It has also been a joy to learn from and work alongside your brilliant students. I am proud to have become an honorary "Peppamer."

I would also like to thank Lidy Fratila-Apachitei for your support and advice throughout the duration of my project. Your guidance has been invaluable, and I am thankful for the many Skype meetings and e-mail exchanges which always helped further my progress.

Thank you to my fellow labmates for their support both in and out of the lab. Thank you to Angela for your fierce dedication to helping me be successful in this project, to Julia for your expert guidance, to John for your passionate discussions and to Marissa, David, Matt, Heidi, Aaliyah, and Drew for creating such a fun and open work environment. Thank you to Camila for allowing me to mentor you and for sharing my excitement about this project.

Thank you to my friends and family for their love and support. Thank you to Firoz and Kate for reassuring me when I felt so far from Delft. Thank you to Pieterjan and Matijs, for being great little brothers and always picking up the phone when I just wanted to chat. Thank you, dad, for your excitement and curiosity about this project and for inspiring me to be an engineer in the first place. A huge thank you to mom for the daily phone calls and making me laugh even when I was overwhelmed with work. And finally, thank you to Justin for being there for me every single day. You are a constant source of motivation – I couldn't have done this without your love and patience.

Abstract

In recent years, bone tissue engineering has emerged as a promising strategy to overcome the limitations of current 'gold standard' treatment options for bone disorders such as bone autografts and allografts. Bone tissue engineering strategies rely on the development of a scaffold that mimics the extracellular matrix, thereby providing an architecture that guides the natural bone regeneration process. Recently, scaffold systems have been developed to incorporate important extracellular signaling molecules which promote fracture healing and bone formation pathways. Among these signaling molecules, naturally occurring growth factors are of particular interest. This interest is due to their ability to enhance cell recruitment and ingress into the scaffold and promote osteogenic differentiation and angiogenesis, each of which is crucial to successful bone regeneration. However, a key challenge in growth factor delivery is that the molecule must reach the site of injury without losing bioactivity and remain in the location for an extended time in order to effectively aid in the formation of new bone. Among various strategies explored in the literature, incorporation of growth factors into particles can offer both protection of bioactivity and a sustained release profile. However, the particles can easily diffuse through the scaffold macropores and traverse to other areas of the body. In this work, a novel two-phase system for the sustained delivery of BMP-2 growth factors has been developed. The system consists of growth factors encapsulated in degradable nanoparticles (nanocarriers) which are immobilized in a porous scaffold. The nanoparticles incorporate a hydrolytically degradable crosslinker that can be easily tuned to achieve desired sustained release profiles. By chemically conjugating the nanocarriers to the scaffold backbone, this two-phase system is able to protect the growth factor from rapid degradation, improve the release kinetics, and achieve longer-term retention within the scaffold. Ultimately, the tunability of this novel growth factor delivery platform can be adapted to a wide variety of applications. Ultimately, this work shows that two-phase systems consisting of growth factor-loaded nanoparticles covalently bound to scaffolds have great promise, both by providing sustained release over a therapeutically relevant timeframe and the potential to sequentially deliver multiple growth factors.

Contents

List of Figures

List of Tables

1 Introduction

Bone-related disorders continue to have a significant effect on people, especially in areas affected by an ageing population [1]. Recent figures suggest that annually over 20 million people worldwide are affected by a lack of bone tissue due to injury or disease, resulting in over 5 million orthopedic procedures annually [2]. For large bone defects which are not capable of self-repair and can occur as a result of traumatic fracture, tumor resection or endoprosthetic loosening, current gold standard treatment options include bone allografts and autografts [3]. Bone autografts rely on the harvesting of bone from another part of the patient's body such as the iliac crest or parts of the tibia [4] and present the advantage of being osteoconductive, angiogenic, and immunocompatible. However, bone autografts can result in a variety of complications including donor site morbidity, infection, pain, and fracture at the donation site [5,6]. Bone allografts, which consist of bone harvested from a donor corpse, eliminate donor site-related complications but present additional challenges such as risk of immune response and transmission of disease. In response to these limitations of current gold standard treatment options, the field of bone tissue engineering has emerged as it presents a promising solution to these limitations.

Bone tissue engineering relies on the use of biodegradable scaffolds which mimics the extracellular matrix and guide the natural bone formation process [7,8]. Successful bone tissue engineering scaffolds present an interconnected porosity, typically with mean pore size around 300 μm [9] as well as mechanical properties such as compressive strength similar to that of native bone. While metals and ceramics have been explored as scaffold materials, natural polymers such as chitosan and their composites have been of particular interest in the development of bone scaffolds due to their inherent biocompatibility and proven osteoconductivity [10].

In addition, recent reports indicate the importance of incorporating signaling molecules into bone tissue engineering strategies in order to enhance the recruitment of cells, osteogenic differentiation and angiogenesis, phases which are crucial to bone tissue regeneration. The different phases of bone healing require the action of a variety of growth factors which include: (i) inflammatory factors which promote the invasion of cells into the scaffold/fracture site, (ii) angiogenic factors which are essential for the vascularization of the new bone, and (iii) osteogenic factors which trigger osteogenic differentiation of mesenchymal stem cells [11].

Of particular interest is a class of growth factors qualified as Bone Morphogenetic Proteins (BMPs) and members of the TGF-beta superfamily [12]. Specifically, BMP-2 and BMP-7 have been identified as playing an important role in osteogenic differentiation. In addition, these factors have been incorporated in FDA-approved commercial systems for spinal fusions [13].

However, the delivery of growth factors for bone tissue engineering applications present major challenges. Growth factors in general and BMP-2 in particular have very short half-lives *in vivo*, often on the order of minutes [14]. These poor pharmacokinetics have led to the delivery of supraphysiological doses which have been shown to lead to side effects such as inflammation, ectopic bone formation and cancer [15]. Therefore, a key challenge is thus to deliver growth factors to the site of injury in a targeted manner without the loss of bioactivity, and to ensure that these growth factors remain at the site of injury for an extended time so as to exert their biological function.

Methods to deliver growth factors in a sustained and controlled way have been widely explored, with a particular interest emphasis on three distinct methods.

- First, the physical entrapment or adsorption of growth factors to the scaffold has been successfully used for burst release of growth factors. However, this method does not allow for sustained delivery of the payload due its rapid diffusion out of the scaffold [16].
- Covalent binding of protein to scaffolds has led to a constant sustained protein release profile. Again, this method fails to prevent the rapid degradation and loss of bioactivity of the protein [17].
- Finally, incorporation of protein into particles has shown great promise for controlled release and is able to both protect the protein and provide a delivery profile consisting of an initial burst release followed by a short, sustained release [18,19]. Unfortunately, as with the method of protein adsorption to the scaffold, this method is likely to produce particles are able to diffuse through the large scaffold pores and be released from the targeted site.

Therefore, this work addresses these challenges and consists of the development of a novel two-phase system for the controlled delivery of growth factors for bone tissue engineering applications (**Figure 1.1**). The system consists of a highly porous chitosan scaffold containing covalently bound, degradable poly(methyl methacrylate-co-methacrylic acid) (P(MMA-co-MAA)) nanoparticles optimized for the delivery of BMP-2. The research has focused on synthesis of chitosan scaffolds, synthesis of

nanoparticles with tunable degradability, loading of protein into the nanoparticles and immobilization of the nanoparticles into the scaffolds.

Chitosan is a natural polymer derived from chitin and primarily found in the exoskeleton of crustaceans [20]. It is widely used for biomedical applications and is of particular interest for bone tissue engineering systems due to its proven biocompatibility, osteogenicity, as well as mucoadhesive properties [10]. In this work, a freeze-drying method was used to synthesize the scaffolds. This method presents distinct advantages such as its ease of implementation, formation of interconnected pores, and anisotropic structure [21].

Poly(methyl methacrylate) (PMMA) is commonly used as a biomaterial, and specifically for tissue engineering applications due to its ease of processing, and low cost [22]. The hydrophobic nature of PMMA has the potential to increase the affinity of nanoparticles for BMP-2 which presents a hydrophobic exterior surface *in vivo*. This further explains its limited solubility in physiological conditions [23]. Further, methacrylic acid (MAA) was incorporated into the nanoparticle backbone in order to introduce reactive carboxyl groups. These reactive carboxyl groups allow for the covalent binding of particles to the chitosan scaffold backbone using carbodiimide crosslinker chemistry.

P(MMA-co-MAA) particles were synthesized using a one-pot UV-initiated emulsion polymerization scheme and through the incorporation of a poly(ethylene glycol) dimethacrylate (PEGDMA) with poly(ethylene glycol) (PEG) molecular weight 600 crosslinker. Subsequently, custom degradable crosslinkers were synthesized by the addition of labile ester bonds in the crosslinker chain. Increasing the number of ester units is believed to increase the hydrolytic degradability of PEG-based hydrogels and could therefore be used to tune the rate of protein release from the particles into the scaffold environment.

Trypsin was used as a model for BMP-2 and the nanoparticles were evaluated for their ability to efficiently load protein. Using a statistical software package, loading conditions were optimized to achieve maximum protein loading efficiency of the system. In addition, this system utilizes a novel method to ensure the sustained retention of protein through the chemical conjugation of nanocarriers to the backbone of the scaffold using carbodiimide crosslinker chemistry. Ultimately, this system seeks to address key challenges in the development of bone tissue engineering scaffolds and aims to present a versatile and robust approach for the controlled delivery of growth factors.

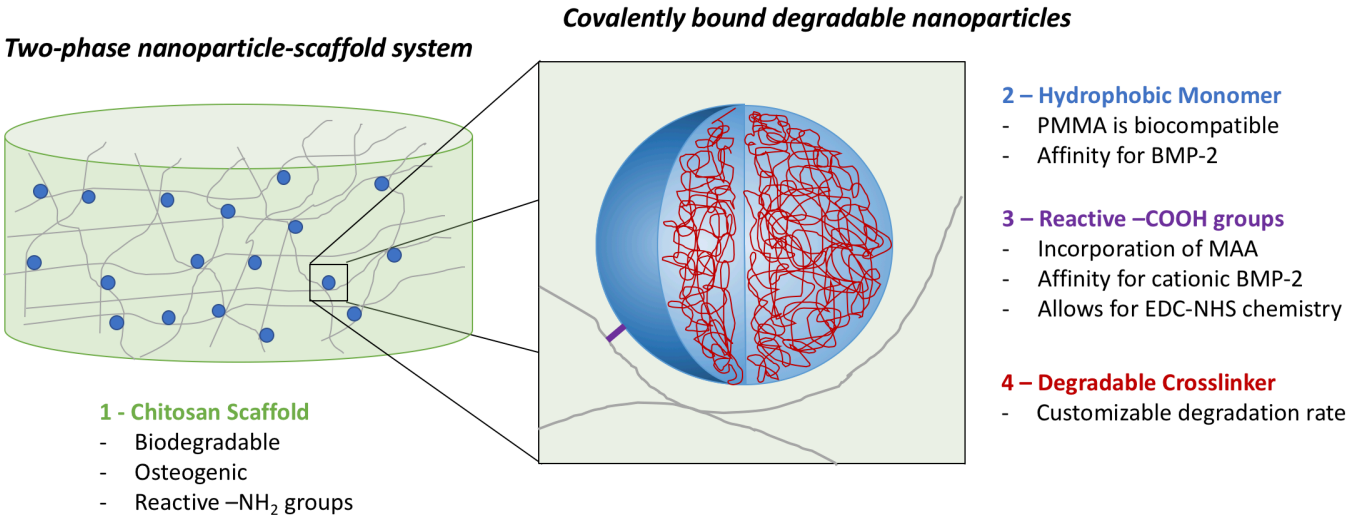

Figure 1.1 - Design of a two-phase nanoparticle-scaffold system for the controlled sustained delivery of BMP-2.

2 Methods

2.1 Materials

Chitosan powder (high molecular weight, weight average molar mass 310-375 kDa, 85% deacetylated, 200-800 cP, Catalog 448877) was obtained from Sigma-Aldrich (Sigma-Aldrich Corporation, St Louis, MO). Acetic acid (glacial, Certified ACS) and sodium carbonate (anhydrous, Powder) were obtained from Thermo Fisher Scientific (Thermo Fisher Scientific, Waltham, MA). Dulbecco's phosphate buffered saline (DPBS) was obtained from Thermo Fisher Scientific.

Methyl methacrylate (MMA, 99%, Catalog M55909) and methacrylic acid (MAA, 99%, Catalog 155721) were obtained from Sigma-Aldrich. Polyethylene glycol dimethacrylate with PEG molecular weight 600 (PEGDMA 600, Catalog 02364) was obtained from Polysciences, Inc (Polysciences, Inc., Warrington, PA). The initiator Irgacure 2959 was obtained from Ciba (Ciba Inc., Basel, Switzerland), while the surfactants Brij 30 and MyTab were obtained from Thermo Fisher Scientific and Sigma-Aldrich, respectively.

D,L-lactide (3,6-Dimethyl-1,4-dioxane-2,5-dione), poly(ethylene glycol) PEG MW=400, poly(ethylene glycol) PEG MW=200, and methacrylic anhydride (containing 2,00 ppm topanol A as inhibitor, 94%) were obtained from Sigma-Aldrich. Hexanes, diethyl ether (99+%, pure, stabilized with BHT), and N,N-dimethylformamide were obtained from Thermo Fisher Scientific, and dichloromethane was obtained from Sigma-Aldrich.

Trypsin from bovine pancreas (powder, Catalog T9201) was obtained from Sigma-Aldrich. DAPI (4'6-diamidino-2-phenylindole, dihydrochloride, Catalog D1306) and FITC (5/6-fluorescein isothiocyanate, Catalog 46425) were obtained from Thermo Fisher Scientific, and tetramethylrhodamine (TAMRA) cadaverine (Catalog 92001) was obtained from Biotium (biotium Inc., Fremont, CA.)

HUV-EC-C (HUVEC) (ATCC CRL-1730) and F-12K Medium (Kaighn's Modification of Ham's F-12 Medium, ATCC 30-2004) were obtained from ATCC (ATCC, Manassas, VA). Heparin sodium (Catalog AC411210010) and fetal bovine serum (Corning, Catalog 35010CV) were obtained from Thermo Fisher Scientific. Endothelial cell growth supplement from bovine neural tissue (ECGS, Catalog E2759) was obtained from Sigma-Aldrich.

2.2 Scaffold Fabrication

Chitosan scaffolds were prepared by dissolving 1, 2, 3 and 4 wt. % chitosan powder (**Figure 2.1**) in 2 vol% (0.34 M) acetic acid. The solutions were placed on a disk rotator and left for 10-12 hours to allow the chitosan to dissolve. A sample of 2.0 mL of the solution was then cast into each well of a 24-well polystyrene plate using a syringe. The plates were then placed in a 37°C incubator overnight. Following incubation, the specimens were collected and immersed in 1 M sodium carbonate solution in order to neutralize acetate functional groups. Subsequently, 0.8 mL of sodium carbonate solution was added to each well and the plates were placed on a plate shaker for 2 h. In order to avoid an excessive amount of sodium acetate salts, excess liquid was removed from the wells. The plates were then frozen at -80°C for 24h. After freezing, the samples were lyophilized in a freeze drier (FreeZone Cascade Benchtop Freeze Dry System, Labconco, Kansas City, MO) under vacuum at -105°C for 48h.

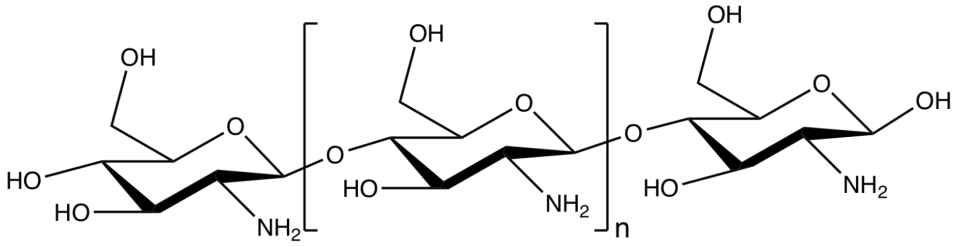

Figure 2.1 - Chemical structure of chitosan

2.3 Scaffold Characterization

2.3.1 SEM Imaging

Scanning electron microscope images were obtained in order to determine the microscopic structure of the lyophilized chitosan scaffolds with varying wt% (1, 2, 3, 4 wt%). Freeze-dried chitosan scaffold samples were sputter-coated with 12 nm of platinum/palladium (Pt/Pd) at 20 mA and imaged by scanning electron microscopy (Supra 40VP SEM, Zeiss, Oberkochen, Germany).

2.3.2 Dynamic Mechanical Properties

In order to understand the behavior of the scaffolds in physiological conditions, the dynamic mechanical properties of the hydrated materials were evaluated. Scaffold storage and loss moduli, G' and G'' respectively, in the hydrated state were determined using a rheometer (Discovery Hybrid Rheometer, TA Instruments, New Castle, DE). Chitosan scaffolds were hydrated in 2.0 mL of 1x

DPBS for 1 hour at room temperature. In order to remove residual sodium acetate salts, the DPBS was replaced three times. With each rinse, the scaffolds were incubated with the fresh DPBS for 1 hour at room temperature and with gentle agitation. A rheometer immersion ring accessory (Peltier Plater Immersion Ring, TA Instruments, New Castle, DE) was used in order to submerge the chitosan scaffolds in 1x DPBS and maintain constant levels of hydration during testing. The linear elastic range of the materials was determined by performing a frequency sweep from 0.01 to 10 Hz at 1% strain. All samples showed purely viscous behavior at frequencies above 0.6 Hz. All subsequent tests were performed at 1% strain from 0.01 to 0.6 Hz. The mechanical properties of scaffolds with increasing wt% chitosan (1, 2, 3 and 4 wt%) (n = 6 per formulation) were compared. Average values and standard deviations were calculated from the measured values at 0.1 Hz. The measured values of the storage modulus correspond to the stored energy and describe the elastic behavior of the material while the loss modulus corresponds to the energy dissipation due to the viscous behavior of the material. The ratio of loss to storage modulus, tan(δ), indicates the relative elastic behavior of the tested material, with values below 1 indicating solid- or gel-like behavior.

2.4 Synthesis of Nanoparticles

Poly(methyl methacrylate-co-methacrylic acid) (P(MMA-co-MAA)) nanoparticles were synthesized using the reproducible method of UV-initiated, aqueous emulsion free radical polymerization [24]. Aqueous emulsion polymerization required the use of hydrophobic monomers, which partitioned into the oil droplet phase. In addition, particle size is controllable by varying the relative amounts of surfactants, initiator, and crosslinking density.

To synthesize the P(MMA-co-MAA) nanoparticles, the prepolymerization mixture was prepared by combining 95 mol% methyl methacrylate, 4 mol% methacrylic acid and 1 mol% poly(ethylene glycol) dimethacrylate (PEGDMA) MW=600 in a round bottom flask. An aqueous solution was formed by adding 25.0 mL of deionized water. In order to form an emulsion, Brij 30, a non-ionic surfactant, and myristyl trimethyl ammonium bromide (MyTAB), a cationic surfactant, were added to the aqueous solution at concentrations of 4 mg/mL and 1.16 mg/mL, respectively. Finally, the free radical initiator Irgacure 2925 was added at a ratio of 0.5 wt%. The chemical structures of the main chemical compounds involved in the emulsion polymerization are shown in **Figure 2.2**.

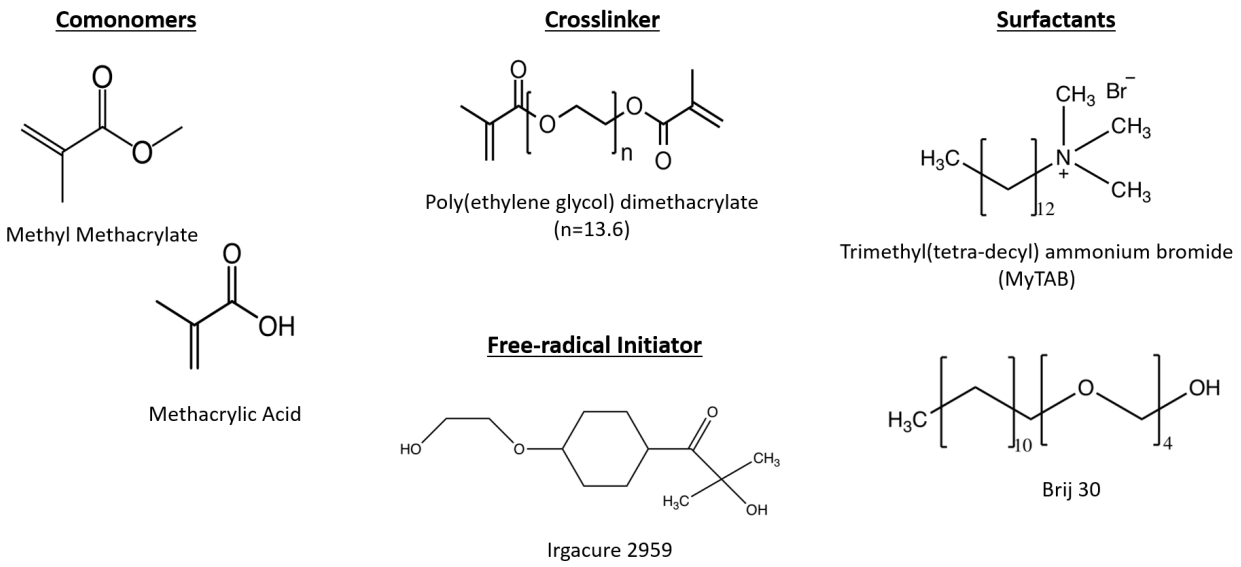

Figure 2.2 – Chemical structures of the comonomers, crosslinker, surfactants and free-radical initiator used for the fabrication of P(MMA-co-MAA) nanoparticles

The reagents were then mixed by ultrasound for 20 minutes in order to form an oil-in-water emulsion, and the emulsion was purged with nitrogen in order to eliminate free radical scavengers. Subsequently, the emulsion was placed under a UV point source with an intensity of 140 mW/cm^2 for 2.5 hours (BlueWave 200 Spot Lamp System, Dymax Corporation, Torrington, CT). The synthesized particles were purified by diluting them at 1:1 in a 6N HCl solution, followed by a dilution at 1:10 in 1x DPBS. The diluted particles were then centrifuged at 4000 g for 5 min so as to form a pellet. The supernatant was then removed, and the nanoparticle pellets were resuspended in 1x DPBS and adjusted to a pH of 7. Finally, the particle solutions were lyophilized under vacuum at -105°C for 48h. The nanoparticle synthesis method is summarized in **Figure 2.3**.

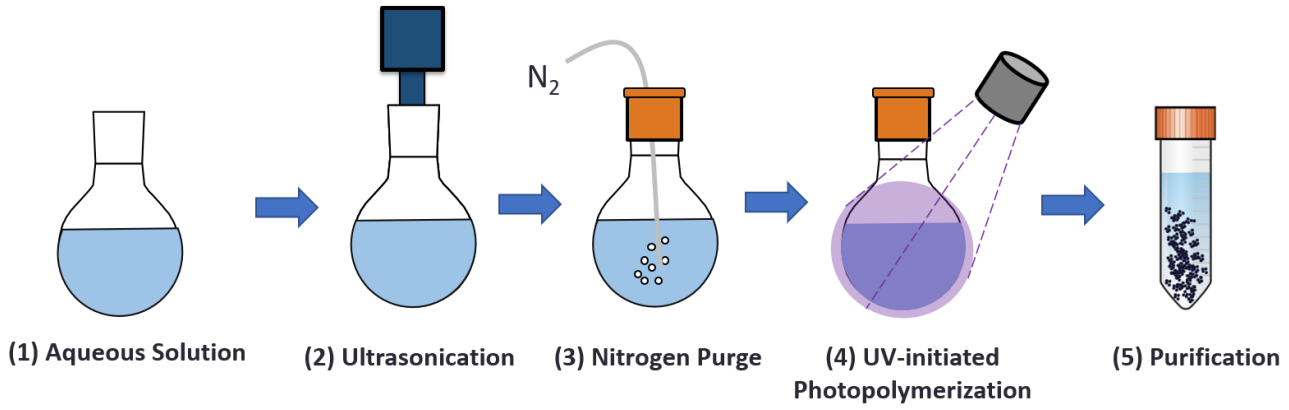

Figure 2.3 - Main steps in the one-pot UV-initiated emulsion polymerization of polymeric nanoparticles. (1) Preparation of the prepolymerization solution, (2) ultrasonication for 20 min to form an oil-in-water emulsion, (3) nitrogen purge to eliminate free radical scavengers, (4) reaction for 2.5 hours, (5) purification by precipitation in acid

After purification, nanoparticle hydrodynamic diameter was determined by dynamic light scattering (Zetasizer Nano, Malvern) using 5x diluted nanoparticle samples in 1x DPBS (n=3 per formulation). In addition, nanoparticle zeta potential was measured as a function of pH in order to determine the net charges present on the particles.

2.5 Synthesis of Degradable Crosslinkers

In order to fabricate hydrolytically degradable nanoparticles, labile ester groups were incorporated along the PEGDMA crosslinker chain. Custom methacrylate-poly(lactic acid)-*b*-poly(ethylene glycol)-*b*-poly(lactic acid)-methacrylate (MA-PLA-b-PEG-b-PLA-MA) crosslinkers were synthesized according to a two-step synthesis originally developed by Hubbell et al. [25] and adapted from Diederich et al. [26], as shown in **Figure 2.4**.

2.5.1 Ring Opening Polymerization of D,L-Lactide on PEG

Poly(ethylene glycol)-co-poly(lactic acid) block copolymer intermediates with varying units of lactic acid were synthesized using a ring-opening polymerization of D,L-lactide on PEG (**Figure 2.4.1**). Diederich et al. reported a conversion of 70% for the incorporation of lactic acid units along the PEG chain [26]. Therefore, in order to load 4 and 8 lactic acid units per PEG chain, 5.6 and 11.2 units of lactic acid were loaded, respectively. In addition, in order to maintain an approximately constant crosslinker length, PEG with lower molecular weight was used for higher numbers of lactic acid units. The amount of D,L-Lactide loaded as well as corresponding molecular weights of PEG used are summarized in **Table 2.1**.

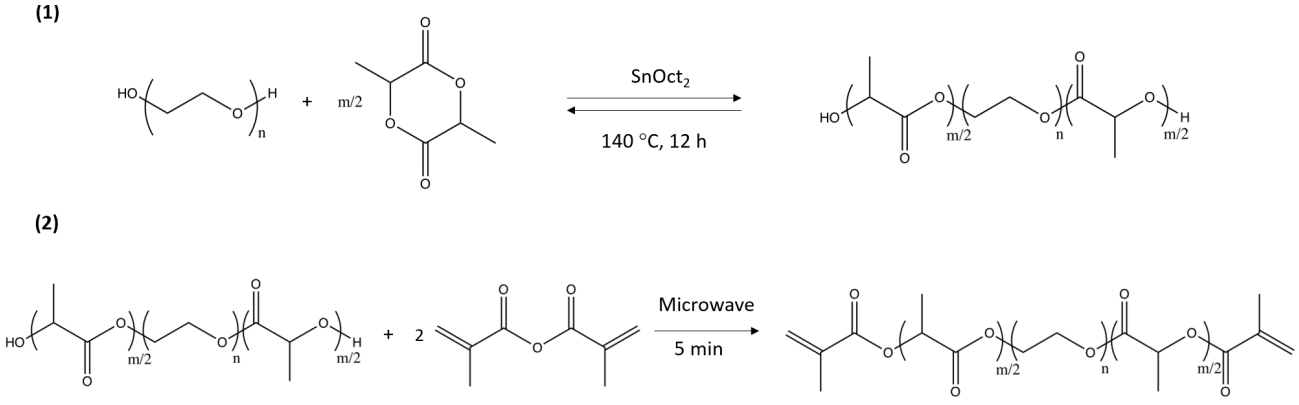

Figure 2.4 - Two step synthesis of custom MA-PLA-b-PEG-b-PLA-MA crosslinker. (1) Ring opening polymerization of D,L-lactide on PEG using stannous octoate (SnOct2) as a catalyst and carried out at 140˚C. (2) Dimethacrylation of PLA-b-PEG-b-PLA intermediate using 10-fold excess of methacrylic anhydride.

Table 2.1 - Ring opening polymerization of D,L-lactide on PEG. Target lactic acid units, moles of reagents used, and final conversions

Target LA units	Loaded LA units	PEG MW	mol PEG	mol D,L-Lactide	Actual m	Conversion
m = 4	5.6	400	0.0125	0.035	4.176	75%
m = 8	11.2	200	0.01	0.056	10.496	94%

In order to load 4 lactic acid units per PEG chain (m=4), 0.0125 mol PEG MW=400 (5 g) and 0.035 mol D,L-lactide (5.045 g) were combined in a 50 mL round bottom flask. The solution was purged with nitrogen for 20 minutes in order to remove oxidizing species. The round bottom flask was then placed in an oil bath and heated to 140˚C. Finally, 0.681 μL of a nitrogen purged stock solution of 10 wt% $SnOct_2$ in toluene was added in order to achieve a ratio of 0.0012 mol $SnOct_2$/mol D,L-lactide. After 12 hours, the reaction was stopped by removing the round bottom flask from the oil bath and the product was allowed to cool to 30˚C. Before solidification, the product was dissolved in 7 mL of dichloromethane. In order to purify the obtained intermediate, the dissolved product was reprecipitated in 400 mL diethyl ether at -80˚C for 6 hours and redissolved in 7 mL of dichloromethane. After a second precipitation cycle, the intermediate was vacuum dried overnight at 40˚C and 28 mmHg, and subsequently stored at 4˚C. The intermediate product was characterized using proton (1H) and carbon (13C) NMR in $CDCl_3$ as well as by FTIR spectroscopy.

2.5.2 Dimethacrylation of PLA-b-PEG-b-PLA Intermediate

Following the synthesis and characterization of the PLA-b-PEG-b-PLA intermediate, a dimethacrylation reaction was carried out, as shown in **Figure 2.4.2**. The dried intermediate and a 10-molar excess of methacrylic anhydride were introduced in a 20 mL capped scintillation vial. The vial was placed in a domestic microwave with the cap loosely twisted. The microwave was set to 5 minutes at maximum power. Every 30 seconds, the vial was removed from the microwave with the cap tightened, and vortexed for 30 seconds. The cap was then loosened again, and the vial placed back into the microwave. These steps were repeated until the vial was microwaved for a total of 5 minutes. The vial was then removed from the microwave and allowed to cool to room temperature with the cap loosened. The cooled methacrylated product was dissolved in 3 mL of dichloromethane and precipitated in 400 mL of hexanes at room temperature for 6 hours. The precipitated product was collected by vacuum filtration using a Buckner funnel and redissolved in dichloromethane. Following

a second precipitation step, the product was dried overnight in a vacuum chamber and stored at 4˚C. The methacrylated custom crosslinkers were characterized using 1H and 13C NMR in $CDCl_3$ as well as FTIR spectroscopy.

2.5.3 Synthesis of Degradable Nanoparticles

The synthesized custom MA-PLA-b-PEG-b-PLA-MA crosslinkers with varying numbers of lactic acid units per chain (m = 4 and m = 10) were incorporated into the UV-initiated emulsion polymerization scheme described in Section 2.4. The synthesized particles were characterized by dynamic light scattering (Zetasizer Nano, Malvern) using 5x diluted nanoparticle samples in 1x DPBS (n=3 per formulation). In addition, the composition of particles with varying number of lactic acid units was compared to the PEGDMA-crosslinked nanoparticles using FTIR spectroscopy.

2.6 Degradation of Nanoparticles

Accelerated hydrolytic conditions were used for all degradation experiments in order to correlate the nanoparticle behavior in experimental conditions to their behavior *in vivo.* Cosgriff-Hernandez et al. established a correlation between the rate of ester hydrolysis in basic conditions and the corresponding hydrolysis rate *in vivo*, concluding that degradation behavior occurring over 1 day at pH 10 and at 37°C in deionized water was equivalent to degradation over 3 weeks in physiological conditions [27]. All experiments were therefore carried out in deionized water or deuterium oxide (D_2O) at 37°C and maintained at a constant pH of 10.

2.6.1 Nanoparticles Count Rate Studies

Particle degradation was first analyzed through the dynamic light scattering derived count rate. The derived count rate corresponds to the theoretical count rate that would be obtained at 100% laser power with zero attenuator and can be used to compare signal strength between samples. For the present system, a decrease in count rate can be linked to the loss of signal associated with particle degradation. Particle degradation profiles were evaluated under accelerated hydrolytic conditions at 37˚C using dynamic light scattering by measuring the change in particle size and count rate over time (Zetasizer Nano, Malvern). Nanoparticles with varying degrees of labile ester bonds along the crosslinker (m=0, 4, 10) were suspended in deionized water at a concentration of 4 mg/mL. Accelerated hydrolytic conditions were achieved by conducting the experiment in an oil bath at 37˚C and under alkaline conditions, using an autotitrator (MPT-2 Autotitrator, Malvern) to maintain a pH value of 10 for the duration of the degradation experiment. At increasing time points throughout the experiment, samples

were analyzed by dynamic light scattering. Due to the aggregation of degradation byproducts, both unfiltered and 0.2 μm-filtered samples were analyzed in order to obtain the count rate for the entire solution and only the non-degraded particles, respectively.

2.6.2 Kinetic NMR Studies

The nanoparticle degradation mechanism relies on the hydrolysis of the ester bonds within poly(lactic acid) units along the crosslinker chain which produces a lactic acid byproduct. The degradation of the P(MMA-co-MAA) nanoparticles can thus be observed via 1H and 13C NMR by analyzing the presence of characteristic peaks for lactic acid in the degradation products, specifically by integrating the doublet centered at 1.21 ppm (ranging 1.20 to 1.22 ppm) characteristic of lactic acid and the quadruplet centered at 1.335 ppm (ranging 1.32 to 1.35 ppm) which corresponds to oligo-lactic acid (OLA).

The particle degradation kinetics were obtained by analyzing the change in NMR spectra of a degrading nanoparticle sample over time. Solutions of nanoparticles (50 mg/mL) with varying degrees of degradable units on the crosslinker (m=0, 4, 10) were prepared in a solution of 0.03 v/v% trimethylsilanol (TMS) in deuterated water (D_2O) and maintained in accelerated hydrolytic conditions (37˚C, pH 10). At given time points (t= 0, 1, 2, 4, 7, 11, 18, 24, 48 h) a sample was obtained from the degradation solution and was analyzed by 1H NMR. The obtained spectra were analyzed by integrating the TMS peak (0 ppm) as well as the range of the spectrum which includes characteristic peaks corresponding to the degradation products (1.55 to 0.5 ppm). This range was selected in order to include, in addition to the characteristic peaks for lactic acid and OLA, peaks which correspond to the methyl protons along the P(MMA-co-MAA) backbone at 0.8 ppm and 1.18 ppm. Since these peaks result in a significant amount of drift from the baseline (after Fourier transform) as well as variability in the degree of baseline drift from sample to sample, integration over this range allows for the normalization of the obtained values. The values obtained by integration were first normalized to the TMS peak. These normalized integral values were then normalized to the maximum peaks at 48 hours, and the percent change in degradation was plotted as a function of time.

2.6.3 Zeta Potential Studies

In order to further characterize the mechanism of degradation and the properties of the degraded nanoparticles, the zeta potential of nanoparticles before and after degradation was measured (Zetasizer Nano, Malvern) at increasing pH values (n=3 for each pH value). The changes in particle zeta potential

with respect to pH were compared between the non-degradable particles and degradable particles before and after degradation.

2.6.4 Imaging of Nanoparticles

Degraded nanoparticle morphology was determined by imaging the particles using transmission electron microscopy (FEI Tecnai Transmission Electron Microscope). Solutions of m=0, 4, 10 nanoparticles both before and after degradation were prepared at 1 mg/mL in distilled water. Samples were negatively stained using 2% PTA (phosphotungstate) at pH 7.0 and prepared on thin bar hexagonal mesh standard thickness, formvar coated copper grids with 600 mesh. The particles were introduced on the grid for 20 seconds and then wicked dry, followed by a 20 second incubation with the stain.

2.7 Protein Loading Study

2.7.1 Selection of Loading Variables

Multiple loading conditions such as temperature, pH, buffer strength, concentrations and incubation length have significant effects on both the protein and particle characteristics and could therefore have a significant effect during protein loading into nanoparticles. In the present study, four key factors were evaluated in order to determine optimal loading conditions to maximize protein loading efficiency.

First, the pH was varied between 4.5, 6, and 7.5. As determined by zeta potential, at pH 4.5 the synthesized particles exhibit significant amounts of aggregation. At pH 6 the particles possess slight negative charges while at pH 7.5, the particles present a net negative surface charge. A further advantage of encapsulating the protein at pH 7.5 would be that the particle-protein system does not undergo any significant shifts due to pH changes after implantation. In addition, it is known that the solubility of BMP-2 around pH 7.5 is limited and that solubility and stability increase with decreasing pH [23]. These phenomena point to the important pH-related tradeoffs with regards to increasing protein loading efficiency.

Second, the protein to particle ratio was varied between 3, 6.5, and 10 wt% (mg protein to 100 mg nanoparticles). A range of protein to particle ratios have recently been reported in the literature with doses varying from 1 to 200 μg/mL [28,29]. In contrast, the BMP-2 dose currently approved for human use range between 1.5 and 2.0 mg/mL [30]. However, it has been shown that these higher doses can

lead to inflammation and diminished quality of the regenerated bone. Evaluating the ability of the particles to load protein at a wide range of weight ratios would allow both for the optimization of the present system as well as an indication of the range of doses that can be delivered by this system for different applications.

In addition, protein was incubated for longer times ranging from 2 hours to 48 hours. Shorter incubation times would present a processing advantage through a reduction in time and cost, whereas increasing incubation time could potentially allow for improved partitioning of the protein into the particles as the system reaches an equilibrium state.

Finally, the total ionic strength of the loading buffer was varied between 5 mM, 15.4 mM, 154 mM. It is known that buffer ionic strength has effect on BMP-2 solubility, with buffer strengths up to 150 mM significantly increasing the solubility of the protein, and above 500 mM leading to the precipitation of the protein [23].

2.7.2 Experimental Design

The selected factors to be evaluated include the incubation time, weight ratio of protein to particle, strength of the buffer in which loading takes place, and pH of the incubation solution. Measuring loading efficiency for these four variables at three levels each requires 81 distinct runs (referred to as 3x3x3x3 Factorial design.) Further, analyzing three replicates per condition would require a total of 243 experiments, resulting in a both costly and time intensive approach to determining optimal loading conditions. In order to reduce the number of runs, a statistical software was used for a design of experiment analysis (JMP, SAS Institute).

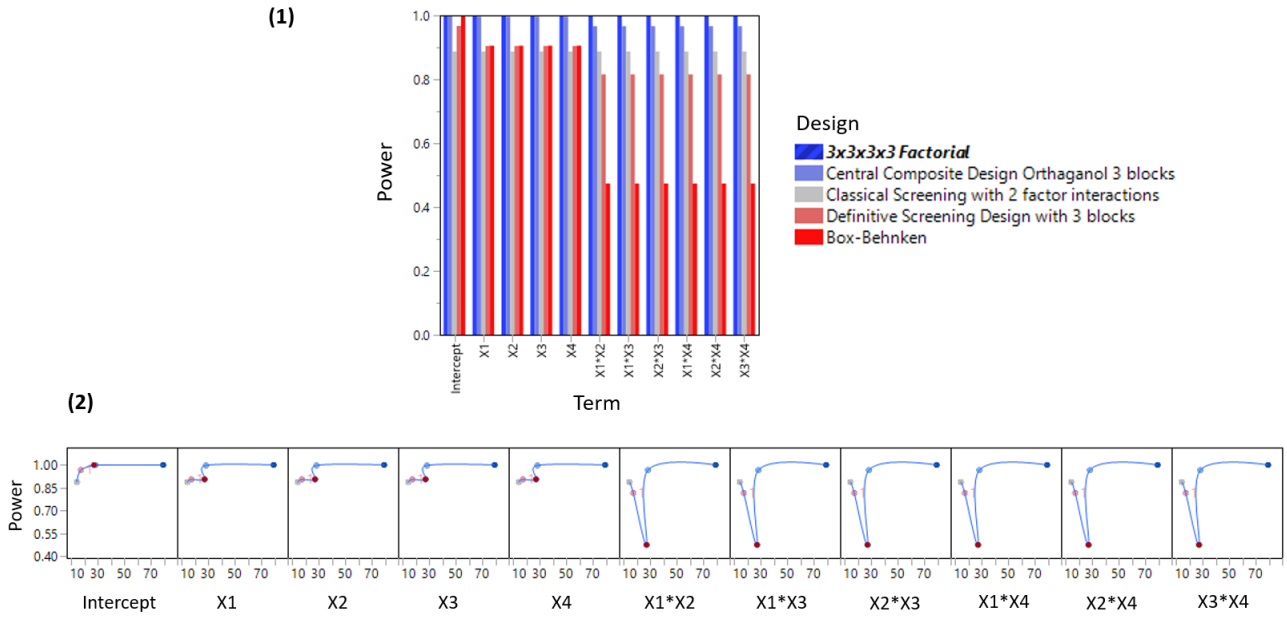

Figure 2.5 - Contrast of experimental designs to the reference 3x3x3x3 factorial design. The power plot (1) shows the statistical power of five distinct experimental designs. The power vs sample size plot (2) shows the number of samples required in order to achieve a given level of statistical power for the different terms.

The key results from the JMP analysis are shown in **Figure 2.5**. **Figure 2.5.1** shows the statistical power of different experimental designs for the 4 terms and 2-factor interactions when compared to the 3x3x3x3 Factorial design, while **Figure 2.5.2** shows the power for different experimental designs as a function of the number of distinct runs required. From the JMP analysis, it can be seen that the Box-Behnken design significantly reduces the number of runs from 81 to 29 runs but has low predictive power for the 2-factor interactions. The Definitive Screening Design requires only 19 runs but similarly has relatively low power for the 2-factor interactions. While the Central Composite design has high predictive power, comparable to that of the 3x3x3x3 factorial design, and requires only 30 runs, it was found that a Classical Screening Design maintains relatively high predictive power for the different variables including 2-factor interactions while requiring only 16 runs. The latter was ultimately selected for its low number of required runs while still maintaining relatively high power. In addition, in order to further improve statistical power, additional runs were included in order to account for any quadratic terms (X_1^2, X_2^2, X_3^2, X_4^2) and provide curvature. Ultimately, 23 loading conditions were tested as detailed in Appendix C.

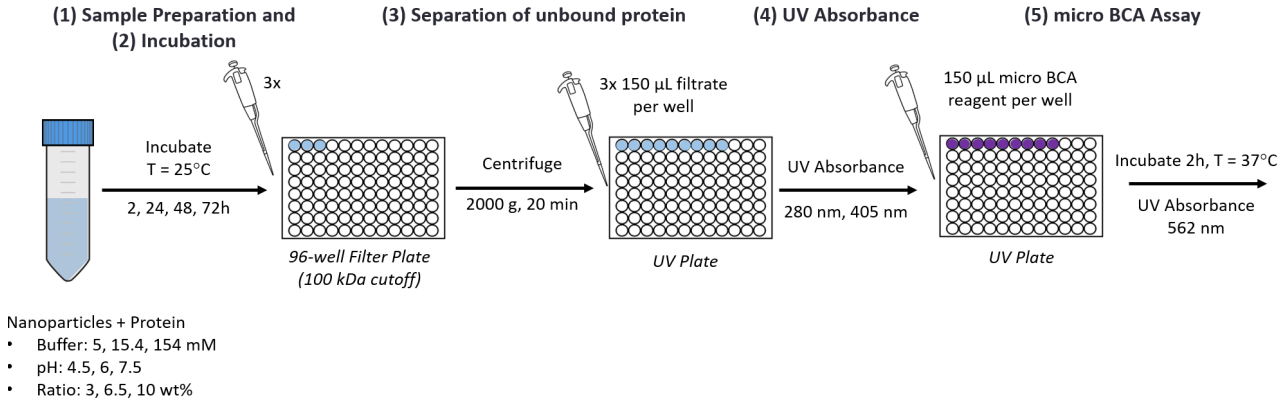

Figure 2.6 - Experimental setup for protein loading experiment. (1) Samples were prepared according to the run description provided by JMP, (2) incubated on a plate shaker at room temperature, (3) pipetted onto a Filter Plate and centrifuged, then (4) filtrate was pipetted onto a UV plate and absorbance spectra were obtained, (5) micro BCA reagent was added to each well of the UV plate, incubated, and absorbance spectra were obtained

2.7.3 Protein Loading Experiment

The proposed system is designed to deliver BMP-2, which is among the most promising growth factors explored for bone tissue engineering applications. BMP-2 has a molecular weight of about 30 kDa and an isoelectric point above 8.5 [23]. In this work, trypsin was selected as a good model for BMP-2 in that it has a similar size of 23.3 kDa, an isoelectric point of 10.8, as well as similar dimensions and comparable stability behavior, with both proteins being most stable around pH 3.

Samples for the protein loading study were prepared as illustrated in **Figure 2.6** and following the formulations outlined in Appendix C.2 by combining different ratios of protein to polymer in different buffers and at different pH conditions. The samples were placed on a plate shaker at room temperature and allowed to incubate for the required incubation time (2, 24, 48, and 72h.) At these respective time points, the corresponding samples were removed from the plate shaker and transferred to a 96-well filter plate (AcroPrep Advance 96 Filter Plate, 100 kDa Omega, Pall.) The membrane cutoff size of 100 kDa was selected such that the particles with bound protein would not be able to traverse the membrane, collecting only the unbound protein. Each loading condition was plated into 3 wells of the filter plate.

The plate was centrifuged at 2000-g for 20 minutes, and the collected samples were transferred to a 96-well UV plate. UV absorption and micro BCA analyses (n=9 per loading condition) were carried out using a microplate reader (Cytation 3 Cell Imaging Multi-Mode Reader, BioTek). UV absorbance values for native trypsin were obtained at 280 nm and 405 nm. Micro Bicinchoninic Acid (BCA)

analysis was carried out by adding microBCA reagent to each well at a 1:1 ratio and incubating at 37°C for 2 hours. The absorbance values at 562 nm were obtained in order to detect the bicinchoninic acid (BCA)/Cu^{1+} complex formed between the reagent and the protein present in the samples. The obtained absorption values were then correlated to values of trypsin concentration using the appropriate calibration curves. The calibration curves for both UV absorption, used for higher concentrations, and microBCA, used for the lower concentration range, are shown in **Figure 2.7**. The measured concentrations correspond to the amount of protein that was not loaded into the nanoparticles and were subtracted from the loaded concentrations in order to determine the amounts of loaded protein for each condition.

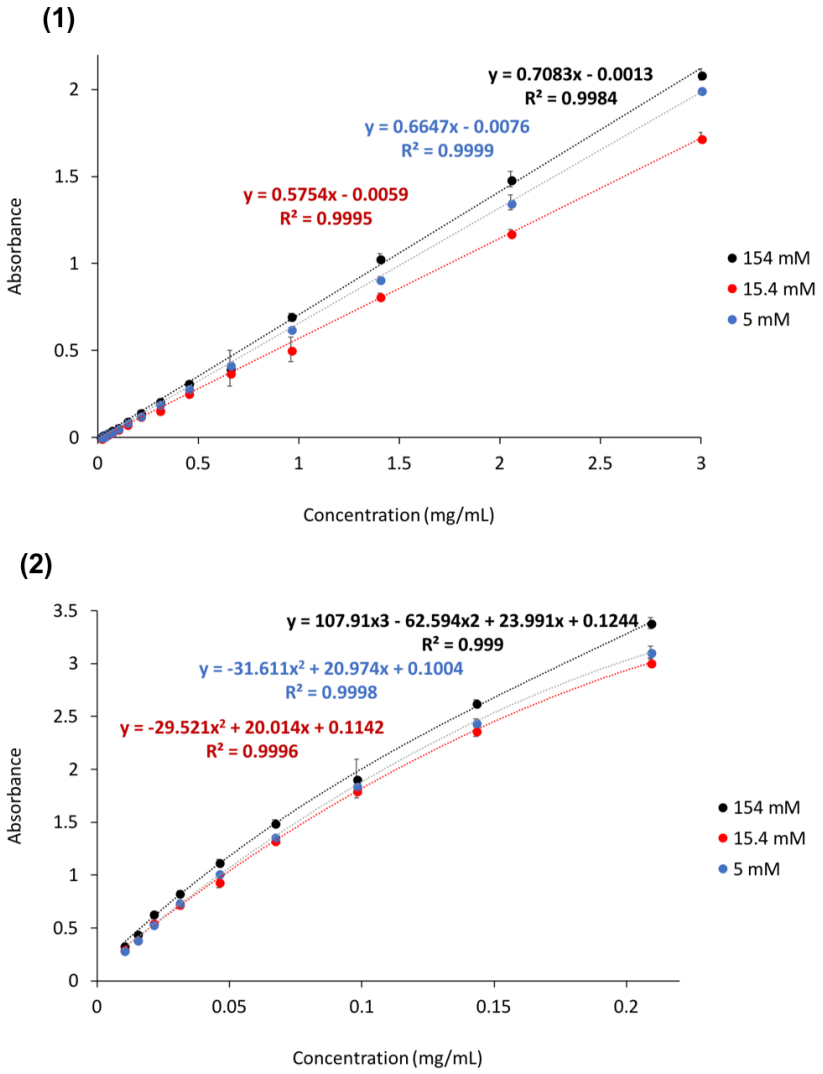

Figure 2.7 - Trypsin concentration calibration curves for (1) UV Absorbance at 280 nm and (2) micro BCA absorbance at 562 nm in 154 mM buffer (blue), 15.4 mM buffer (orange), and 5 mM buffer (grey)

2.8 Particle Immobilization to the Scaffold Backbone

A fluorescent imaging study was carried out in order to test the hypothesis that the adsorption of protein or particles within scaffolds can lead to their rapid diffusion out of the scaffold bulk. In addition, this study sought to identify whether the chemical conjugation of nanoparticles to the scaffold backbone would immobilize them within the scaffold for an extended time. Three distinct systems were compared: (system I) free protein adsorbed to the scaffold, (system II) free nanoparticles simply entrapped in the scaffold, and (system III) nanoparticles immobilized to the scaffold by carbodiimide crosslinker chemistry between the carboxylic acids on the surface of the nanoparticles and the primary amines on the chitosan scaffold backbone.

Each component of the system was first labelled with a distinct fluorescent dye. Chitosan scaffolds were labelled using fluorescein isothiocyanate (FITC) (green fluorescent dye) by forming a urea bond with the primary amine groups on the scaffold backbone. A 10 mg/mL solution of FITC in DMF was added to each scaffold at a ratio of 0.067 v/v% FITC to scaffold. Trypsin was labelled using 4',6-diamidino-2-phenylindole, dihydrochloride (DAPI) (blue fluorescent dye). A 10 mg/mL solution of DAPI in deionized water was added to a solution of trypsin at a ratio of 0.22 mg DAPI/mg trypsin. Finally, P(MMA-co-MAA) nanoparticles were labelled using tamra cadaverine (red fluorescent dye). A 70 mg/mL solution of tamra cadaverine in ethanol was added to a 10 mg/mL solution of nanoparticles at a ratio of 5 mg tamra cadaverine/mg nanoparticles.

After fluorescent labelling, the three distinct systems were prepared. For system I, DAPI-labelled trypsin was loaded into the scaffolds by incubating the scaffold in protein solution similar to the adsorption loading methods existing in the literature. Protein was loaded at a concentration of 1 mg per mL of scaffold, concentrations which are commonly used for similar systems in the literature as well as commercially available systems. For system II, nanoparticles were loaded into the scaffold at a concentration of 100 μL nanoparticle solution /mL scaffold using a 2 mg/mL stock solution of P(MMA-co-MAA) nanoparticles. Finally, for system III carbodiimide crosslinker chemistry was used to bind the carboxylic groups on the nanoparticles to the primary amines of the chitosan backbone and nanoparticles were loaded at the same ratio as in system II. This was done by first activating the tamra cadaverine-labelled nanoparticles using 1-ethyl-3-(3-dimethylaminopropyl) carbodiimide hydrochloride (EDC) and sulfo-N-hydroxysulfosuccinimide (NHS). A 2 mg/mL solution of nanoparticles was prepared by combining stock solutions of EDC in ethanol, sulfo-NHS in ethanol and the labelled nanoparticles in 1x DPBS at a mass ratio of 0.4:1.1:0.5. The solution was adjusted to

pH 6 and maintained at room temperature for 15 minutes to allow for the activation reaction with EDC and sulfo-NHS. The solution was then adjusted to pH 7.2 and 200 μL was added to each scaffold. The scaffolds were maintained at pH 7.2 and at room temperature to allow for the reaction of sulfo-NHS activated nanoparticles with the primary amines on the scaffold backbone. After 10 hours, the scaffolds were washed with fresh 1x DPBS and stored at room temperature.

The labelled systems were then incubated in DPBS for up to 4 weeks. In order to mimic the fluid flow in the body, washes were performed every 5 minutes for the first 30 minutes of incubation followed by every 30 minutes for the following 3 hours. Fluorescent images were obtained using a manual inverted microscope (IX73, Olympus) using the phase contract to visualize the naked scaffold, DAPI filter to visualize the labelled protein, GFP filter to visualize the labelled scaffold backbone, and RFP filter was used to visualize the labelled nanoparticles. Images were obtained immediately after loading, after 30 min, 72 hours, and after 4 weeks in order to determine the relative change over time in protein for system I and particles for systems II and III.

2.9 In vitro *Studies: Cell Viability and Proliferation*

2.9.1 Cell Culture

The biocompatibility of the two-phase scaffold-nanoparticle system was analyzed using non-immortalized human umbilical vein endothelial cells (HUVEC). Cells were propagated for two passages using a F-12K Medium with 0.1 mg/mL heparin, 1 v/v% endothelial cell growth supplement, and 10 v/v/% fetal bovine serum.

Four systems were evaluated for cytotoxicity: (I) P(MMA-co-MAA) nanoparticles with m = 0, m = 4, and m = 10 crosslinkers, (II) degraded P(MMA-co-MAA) nanoparticles with m = 0, m = 4, and m = 10 crosslinkers, (III) 2 wt% chitosan scaffolds, and (IV) covalently bound P(MMA-co-MAA) nanoparticles to 2 wt% chitosan scaffold.

Cell culture treated 96-well plates were coated with 50 μL of a 1:100 fibronectin solution in 1x DPBS and incubated at room temperature for 1 hour. The fibronectin solution was then removed from the plate and the wells were rinsed with DPBS. HUVEC cells were then seeded at 3000 cells per well and allowed to incubate at room temperature for 1 hour. Cells were then incubated for 24 hours in a humidified environment at 37°C and 5% CO_2.

For systems III and IV, the scaffolds were introduced into the wells prior to cell seeding in order to allow for improved contact between the cells and scaffold. Scaffolds were sectioned into 3 mg pieces, sterilized by UV exposure, and incubated in HUVEC media overnight prior to being placed in the wells. For system IV, 2 wt% chitosan scaffolds with covalently bound particles at a concentration of 0.2 mg/mL nanoparticle to scaffold were used.

For systems I and II, solutions of P(MMA-co-MAA) nanoparticles with m = 0, m = 4 and m = 10 crosslinkers and solutions of degraded nanoparticles were prepared. These solutions were diluted in HUVEC media, and 5 μL was added to each well in order to achieve final concentrations of 0.01, 0.02, 0.5, and 1 mg/mL. Positive and negative controls were prepared by incubating cells in HUVEC media (positive control) and with both triton and SDS (negative lysis controls). All systems were subsequently cultured for 24 and 48 hours in a humidified environment at 37°C and 5% CO_2.

2.9.2 MTS Cell Proliferation Assay

Cell proliferation in the presence of the system components after 24 and 48 hours was determined using an MTS cellular proliferation assay and used as an indicator of cell health. The CellTiter 96 AQueous One Solution Cell Proliferation Assay (Promega Corporation, Madison, WI) was used per manufacturer's instructions, and the resulting absorbance of the plate at 490 and 690 nm was obtained. Relative cellular proliferation was calculated by first subtracting the background absorbance at 690 nm from the absorbance at 490 nm. Subsequently, the obtained values were normalized to the average absorbance of the positive and negative controls (HUVEC cells in the HUVEC media and lysis control, respectively) in order to obtain the average cell proliferation for each condition (n=6 per condition.)

2.9.3 LDH Membrane Integrity Assay

Cell membrane integrity in the presence of the system components after 24 and 48 hours was determined using a lactose dehydrogenase (LDH) membrane integrity assay as an indicator of cell health. The Promega CytoTox-ONE Homogeneous Membrane Integrity Assay (Promega Corporation, Madison, WI) was used per manufacturer's instructions. The resulting fluorescence of the samples was measured at an excitation of 560 nm and an emission of 590 nm. Background fluorescence values as a result of the cell culture media were first subtracted from the obtained fluorescence values. These were then normalized to the average maximum LDH release (lysis control) and minimum LDH release (media control) in order to obtain the average cell viability for each condition (n=6 per condition.)

3 Results

3.1 Scaffold Properties

Chitosan scaffolds with varying wt% of chitosan were prepared in order to optimize the fabrication of scaffolds to be used in the proposed system. The rheometry data shown in **Figure A.1** suggests that an increase in wt% of chitosan has a slight effect on the storage and loss moduli of the materials, increasing from 6900 to 9100 Pa and decreasing from 628 to 551 Pa, respectively. However, an increase in chitosan wt% results in a noticeable increase in the viscosity of the chitosan solution. Because the scaffold fabrication process requires the casting of chitosan solution into molds, increased viscosity can result in a loss of material and the introduction of large air bubbles. It was therefore found that a 2 wt% formulation provided the best trade-off between higher mechanical properties and ease of handling.

Scanning electron microscope images indicate that a highly porous network was formed within the scaffold bulk (**Figure 3.1**). A hierarchical structure is observed, with smaller pores of around 300 μm in diameter as well as the presence of macropores. In addition, an anisotropic structure is observed, with pores oriented orthogonally to the image plane. This direction coincides with the direction of solvent sublimation during the freeze-drying process as well as the direction of loading during dynamic mechanical testing.

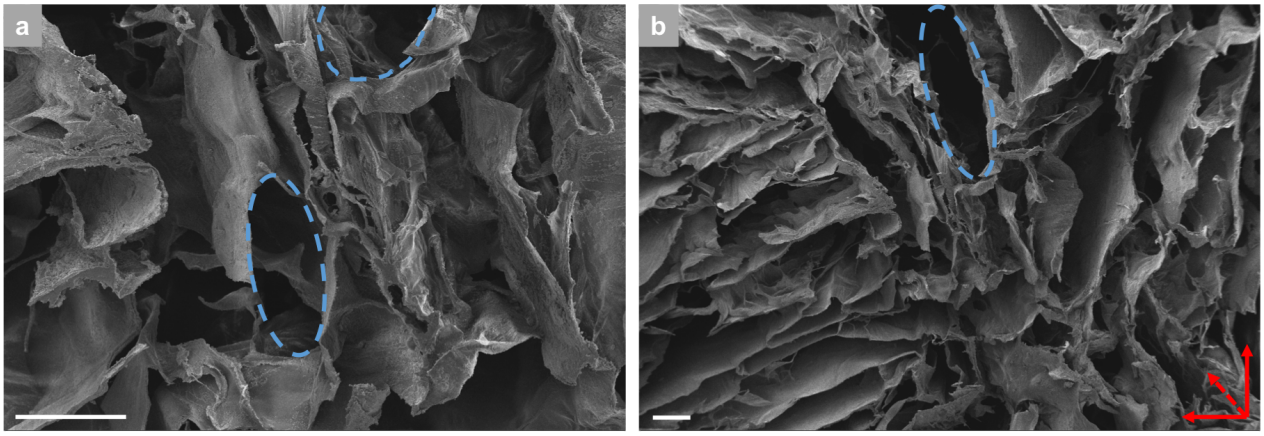

Figure 3.1 - Scanning electron microscope images of 2 wt% chitosan scaffolds at (a) 300x magnification and (b) 100x magnification. Scale bars = 200 μm. Blue dotted lines indicate visible pore structures while red dotted arrow indicates pore direction

The rheology data obtained for the chitosan scaffolds indicated that the 2 wt% chitosan scaffolds present a storage modulus (G') of around 8300 Pa and a loss modulus (G'') of 606 Pa with a tan(δ) of 0.085 (Appendix A.1). These values indicate that the fabricated scaffolds, despite a high porosity behave largely like gels as opposed to viscous materials with the elastic component having a greater influence on the material behavior.

3.2 Nanoparticle Synthesis

The UV-initiated emulsion polymerization scheme allowed for the synthesis of nanoparticles with hydrodynamic radii between 60 and 80 nm (**Figure 3.2**). In addition, the particles were relatively monodisperse, with polydispersity indices around 0.170. Finally, comparing the properties between batches, the present particle synthesis scheme led to minimal batch-to-batch variability and provided a reproducible method for the synthesis of P(MMA-co-MAA) particles.

The synthesized particles present a zeta potential of around -22 mV at physiological pH, indicating that the particles carry a net negative charge and form a stable suspension in these conditions (**Figure 3.3**). In increasingly acidic environments, the particle zeta potential increases towards 0 mV with an observed pKa of 3.50, resulting in a reduction of net charges and therefore decreased ability for repulsion between particles. This decreased ability for repulsion leads to the aggregation of particles as pH is decreased, as illustrated in **Figure 3.3.2**. While particle sizes remain below 100 nm at pH values above 7, the recorded hydrodynamic diameter progressively increases as pH is reduced reaching values of up to 13 μm. This increase reflects the formation of micron-scale aggregates as the particle net surface charge decreases. Furthermore, it was shown that this aggregation of particles as a result of a decrease in pH is a reversible phenomenon (Appendix B.1).

(1)

Batch #	Average diameter (nm)	PDI
1	60.36	0.165
2	76.05	0.176
3	64.89	0.167

(2)

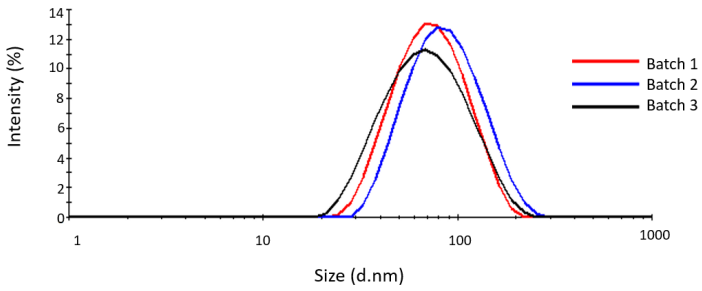

Figure 3.2 - Dynamic light scattering results of nanoparticles synthesized using a one-pot UV-initiated emulsion polymerization. (A) Batch to batch variability of the average hydrodynamic diameter of the nanoparticles and respective polydispersity indices. (B) Plot of the intensity distribution of hydrodynamic diameters for different batches.

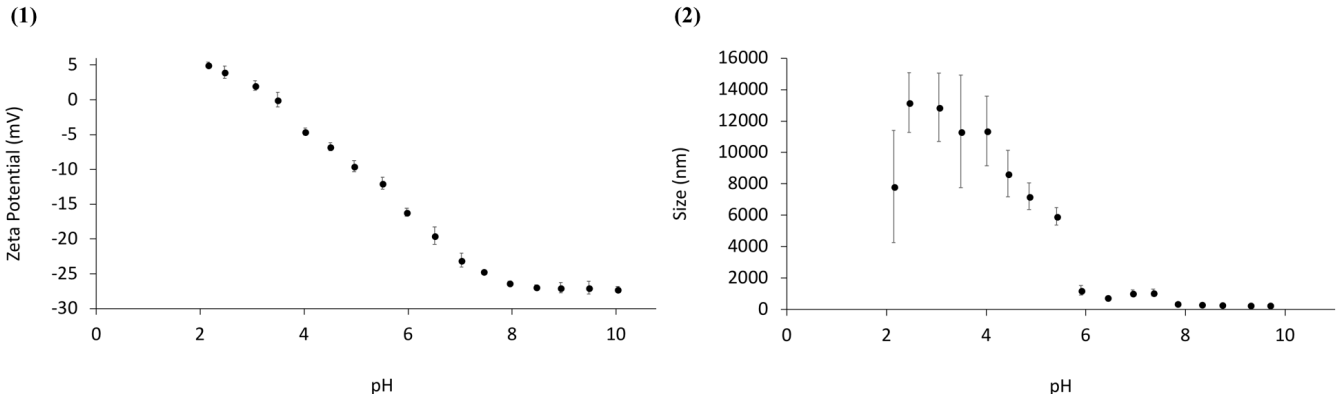

Figure 3.3 – (1) Zeta potential and (2) particle size as a function of pH for P(MMA-co-MAA) nanoparticles

3.3 Synthesis of Degradable Nanoparticles

The custom MA-PLA-b-PEG-b-PLA-MA crosslinkers synthesized according to the procedure in Section 2.5 were characterized using 1-H NMR (**Figure 3.4**) in order to confirm the successful incorporation of PLA units and methacrylation of the end groups of the chains. The PEGDMA 600 MW crosslinker used for the non-degradable particles presented a tall peak at 3.6 ppm (peak e) characteristic of the PEG units [26]. This spectrum additionally revealed three characteristic peaks for the two methacrylate ends observed at 1.8, 5.7, and 6.2 ppm (peaks f, b, and a, respectively). Finally, a peak is observed at 4.25 ppm (peak d) which is characteristic of the presence of a carbon bond to the PEG repeating units. Notably, this peak does not appear on the spectrum of the non-methacrylated PEG as shown in Appendix **Figure D.1**, suggesting that this peak appears due to the bond between the repeating unit and the methacrylate ends. The spectra of the m=4 and m=10 custom degradable crosslinkers presented these same five peaks with additional peaks at 1.5 ppm (peak g) and 5.2 ppm (peak c), characteristic of the lactic acid units.

From the NMR spectra, a decrease in the height of the PEG peak (peak e) can be observed as the number of degradable units on the crosslinker is increased. This is attributed to use of 400 and 200 MW PEG for the m = 4 and m = 10 crosslinkers, respectively in order to maintain a constant crosslinker length. In addition, the areas under peaks c and g increase between m = 4 and m = 10 due to the presence of a greater number of lactic acid units. Finally, peaks a and b which correspond to the methacrylate ends of the polymer chains remain similar for all three crosslinker formulations. This is due to the fact that each crosslinker chain, regardless of number of lactic acid units or length of the PEG chain, presents two methacrylate groups, one on each end. Finally, quantitative analysis of the

NMR spectra confirms the presence of 2 methacrylate groups per chain, an average of 4.2 lactic acid units per chain for m = 4, and 10.5 lactic acid units per chain for m = 10.

Nanoparticles fabricated with the custom crosslinkers presented similar hydrodynamic diameters to those fabricated with the non-degradable PEGDMA 600 MW (**Figure 3.5**) with average diameters ranging between 57 and 86 nm when compared to 65 nm for the non-degradable particles. Batch to batch variability remained small, though an increase in polydispersity indices to about 0.200 and 0.300 was observed for nanoparticles fabricated with the m = 4 and m = 10 custom crosslinkers, respectively.

Comparison of the FTIR spectra of the degradable nanoparticles to the non-degradable nanoparticles confirms the successful incorporation of the custom crosslinkers (**Figure 3.6**). When comparing the spectra for increasing number of incorporated lactic acid units, an increase is observed in the peaks at around 1750 cm^{-1} which correspond to the carbonyl stretching of the PLA units in the crosslinker. In addition, peaks at around 1450 cm^{-1} and 1350 cm^{-1} are observed and correspond to the asymmetric and symmetric bending of the methyl groups of the PLA units, respectively. Finally, a peak is identified at around 1180 cm^{-1} which corresponds to the C-O stretching of the PLA units. An increase in these peaks for increased number of lactic acid units incorporated in the custom crosslinkers confirms the successful incorporation of these degradable crosslinkers in the synthesis of nanoparticles.

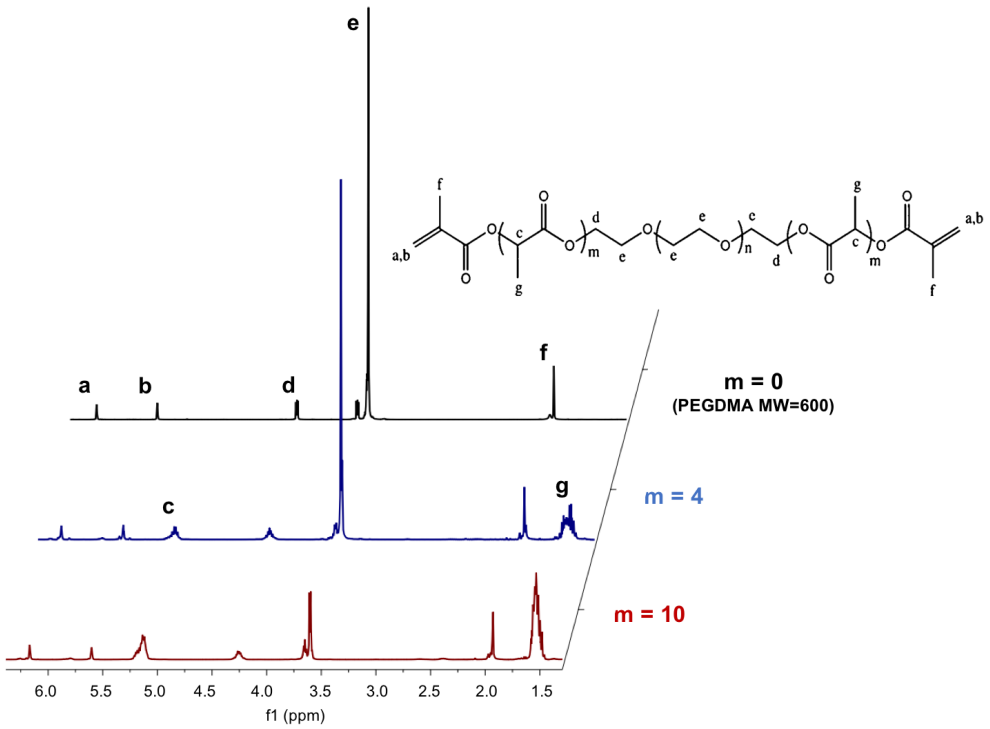

Figure 3.4 - Comparison of the 1H-NMR spectra for a PEGDMA MW=600 crosslinker without incorporated degradable units (black), the custom crosslinker with 4 lactic acid units incorporated per PEG MW=400 chain (red), and the custom crosslinker with 10 lactic acid units incorporated per PEG MW=200 chain (blue)

(1)

Crosslinker PLA units	Average diameter (nm)	PDI
m=0	64.89	0.167
m=4	86.26	0.227
m=10	57.46	0.315

(2)

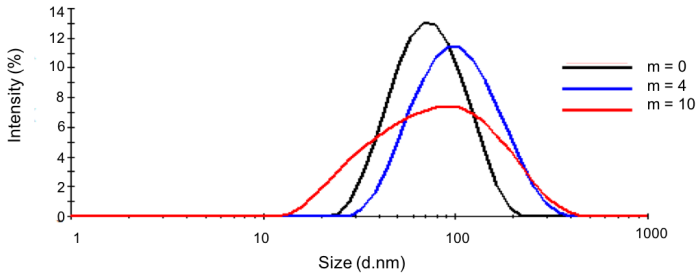

Figure 3.5 - Dynamic light scattering results of P(MMA-co-MAA) nanoparticles synthesized using a one-pot UV-initiated emulsion polymerization using either: a PEGDMA MW=600 crosslinker (m=0), a MA-PLA-b-PEG-b-PLA-MA custom crosslinker with 4 lactic acid units (m=4) or 10 lactic acid units (m=10)

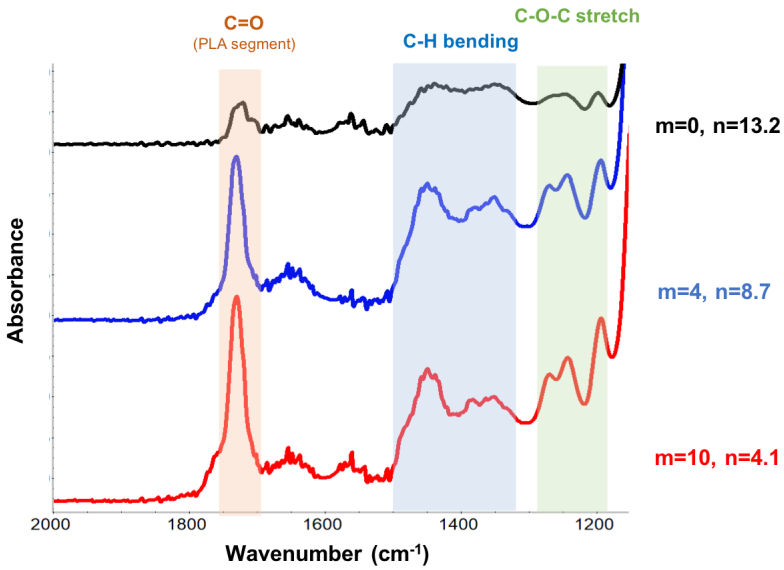

Figure 3.6 – FTIR spectra of nanoparticles fabricated with non-degradable crosslinker (m = 0, black) and custom degradable crosslinkers with 4 and 10 lactic acid units per chain (m = 4, blue and m = 10, red, respectively)

3.4 Degradation of Nanoparticles

As is demonstrated by the change in relative count rate over time (**Figure 3.7**), nanoparticles fabricated with the custom crosslinkers exhibit degradation behavior when maintained at pH 10 and 37°C. Indeed, in the first 24 hours a significant reduction in the count rate is observed, with the count rate reduced by half within 4.5 hours for particles fabricated with the m=4 crosslinker and within 1.5 hours for particles fabricated with the m=10 crosslinker. In addition, both particle formulations continued to see a decrease in count rate over time and reached a plateau after around 48 hours for m=4 and 28 hours for m=10. Overall, a more rapid rate of reduction in count rate was observed for the m=10 nanoparticles. The non-degradable nanoparticles do not exhibit this decrease in count rate as a function of time and in fact show a slight increase in count rate after 6 hours followed by a plateau, which can be explained by an initial swelling behavior due to delayed hydration of the nanoparticles.

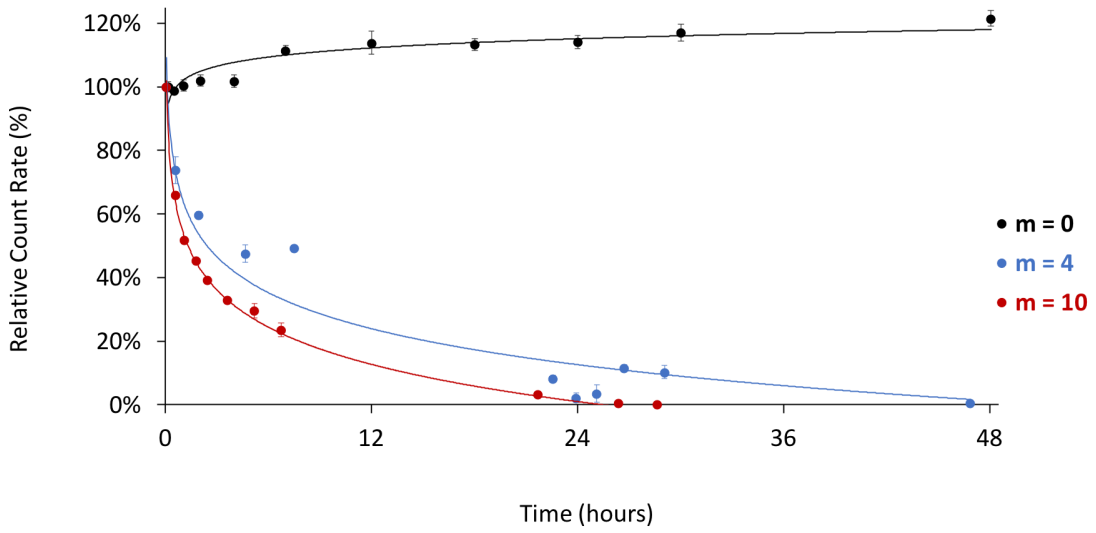

Figure 3.7 - Plot of relative count rate as a function of degradation time for nanoparticles with a non-degradable crosslinker (m=0, black), m=4 crosslinker (red) and m=10 crosslinker (blue) normalized to the initial and final count rate values

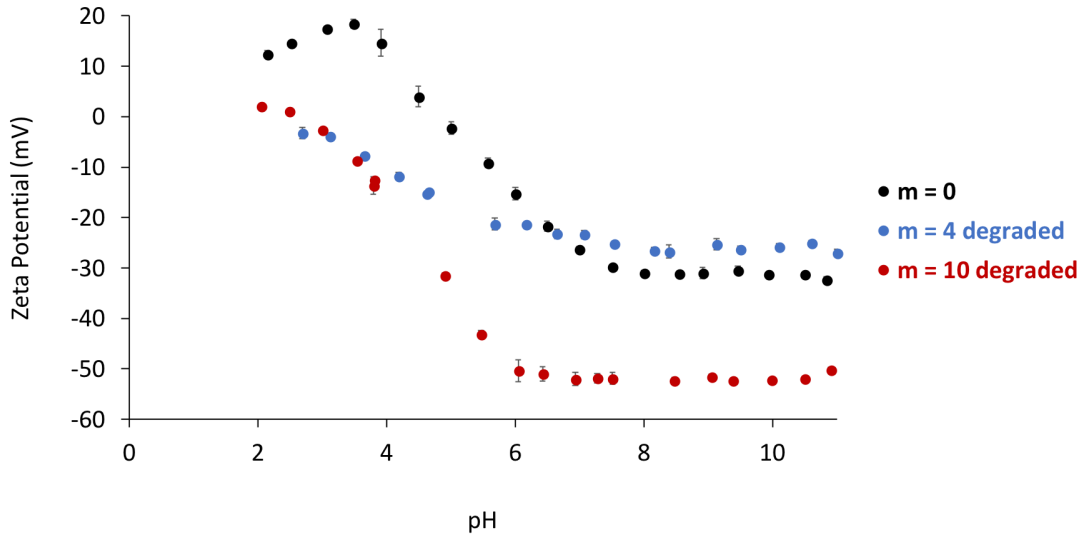

Figure 3.8 - Zeta potential as a function of pH at 25C for degraded particles with increasing number of degradable units along the crosslinker chain

Degraded nanoparticles showed significant change in charge behavior as a function of pH (**Figure 3.8**). Both the degraded m=4 and m=10 particles exhibit different zeta potential trends as a function of pH when compared to the non-degradable particles after being subjected to accelerated degradation conditions for 48 hours. The degraded particles begin to present negative surface charges at lower pH values, with the observed pKa value being shifted from 4.5 for m = 0 to about 2.5 for m = 10. The hydrolytic degradation of poly(lactic acid) units results in the formation of acidic byproducts [31] which can explain the onset of negative charges in lower pH ranges for the degraded nanoparticles.

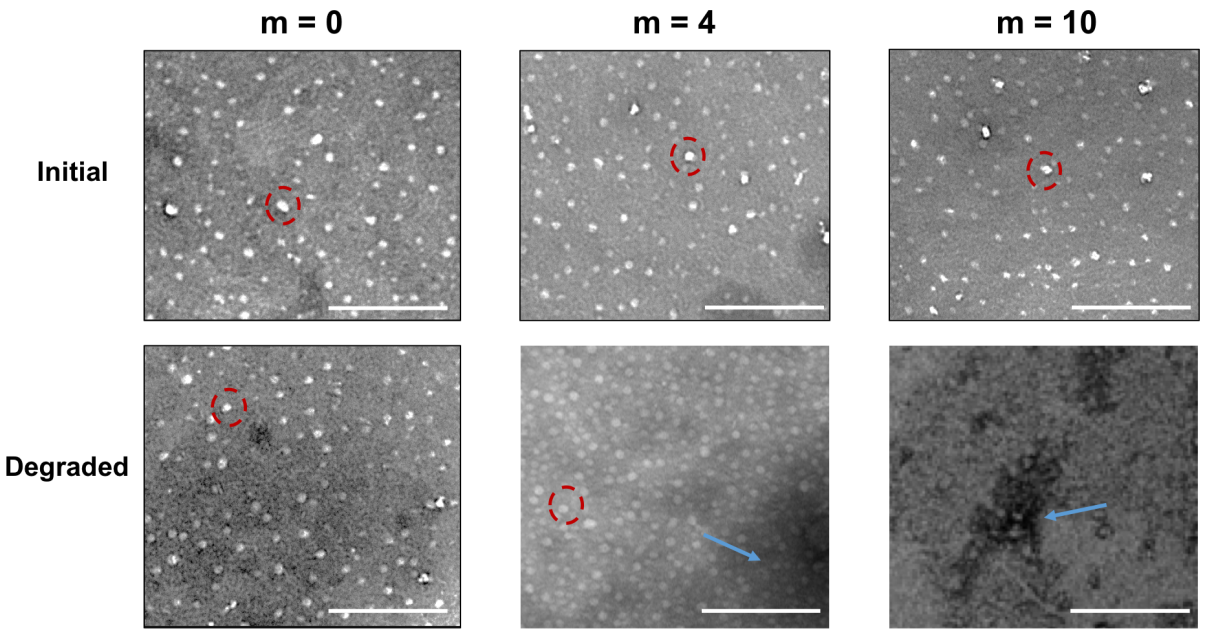

Figure 3.9 – Transmission electron microscope images of m = 0, m = 4 and m = 10 nanoparticles before and after degradation. Scale bars: 200 μm. Examples of intact particles are indicated by the dotted red lines while degraded polymer is indicated with the blue arrows.

A change in nanoparticle morphology was also observed between the initial non-degraded nanoparticles, and the nanoparticles subjected to accelerated degradation conditions. The m = 0, m = 4, and m = 10 nanoparticles all presented similar morphologies in their initial state, as indicated by the white spheres present in the top images of **Figure 3.9**. After incubation at 37°C and pH 10, the m = 0 nanoparticles showed no significant change in morphology. However, a reduction in the number of visible nanoparticles was observed for m = 4 and m = 10, with the appearance of large aggregates of linear polymer and degradation byproducts. In addition, when comparing the degraded m = 4 and m = 10 particles, the m = 4 sample showed the presence of a small number of intact particles, whereas the intact particles for m = 10 were no longer detectable.

Furthermore, NMR spectra of the nanoparticles subjected to accelerated degradation conditions obtained at different time points throughout degradation process reveal an increase in degradation products over time (**Figure 3.10.1**). The spectra of the m = 0 nanoparticles show minimal change over time with a slight increase in the 1.18 ppm peak over time. This increase can be explained by the slow degradation of ester bonds along the PEG units, which may also appear at the 1.18 ppm peak. On the other hand, the spectra for the m = 4 and m = 10 nanoparticles reveal a distinct change over time, with the appearance of a quadruplet around 1.33 ppm and a doublet at 1.20 and 1.22 ppm and their visible increase in height as a function of time. It can also be qualitatively observed that the increase in these

peaks is more rapid and significant for the m = 10 nanoparticles. A quantitative analysis of these spectra (**Figure 3.10.2**) reveals this difference in degradation rate. It is found that the m = 4 nanoparticles follow a third order polynomial degradation profile, with 50% degradation after 11 hours and 100% degradation after 48 hours. The m = 10 nanoparticles follow a fourth order polynomial degradation profile and reach 50% degradation after about 6 hours and 100% degradation after 24 hours. In contrast, the slight degradation behavior observed for the m = 0 nanoparticles occurs on an entirely different time scale, with under 10 % degradation after 48 hours. Comparing these experimentally obtained degradation profiles carried out in accelerated degradation conditions to the corresponding behavior *in vivo* as defined by Cosgriff-Hernandez et al. [27], it was found that the m = 4 nanoparticles would be fully degraded after 6 weeks *in vivo* whereas the m = 10 nanoparticles would be fully degraded after 3 weeks *in vivo.*

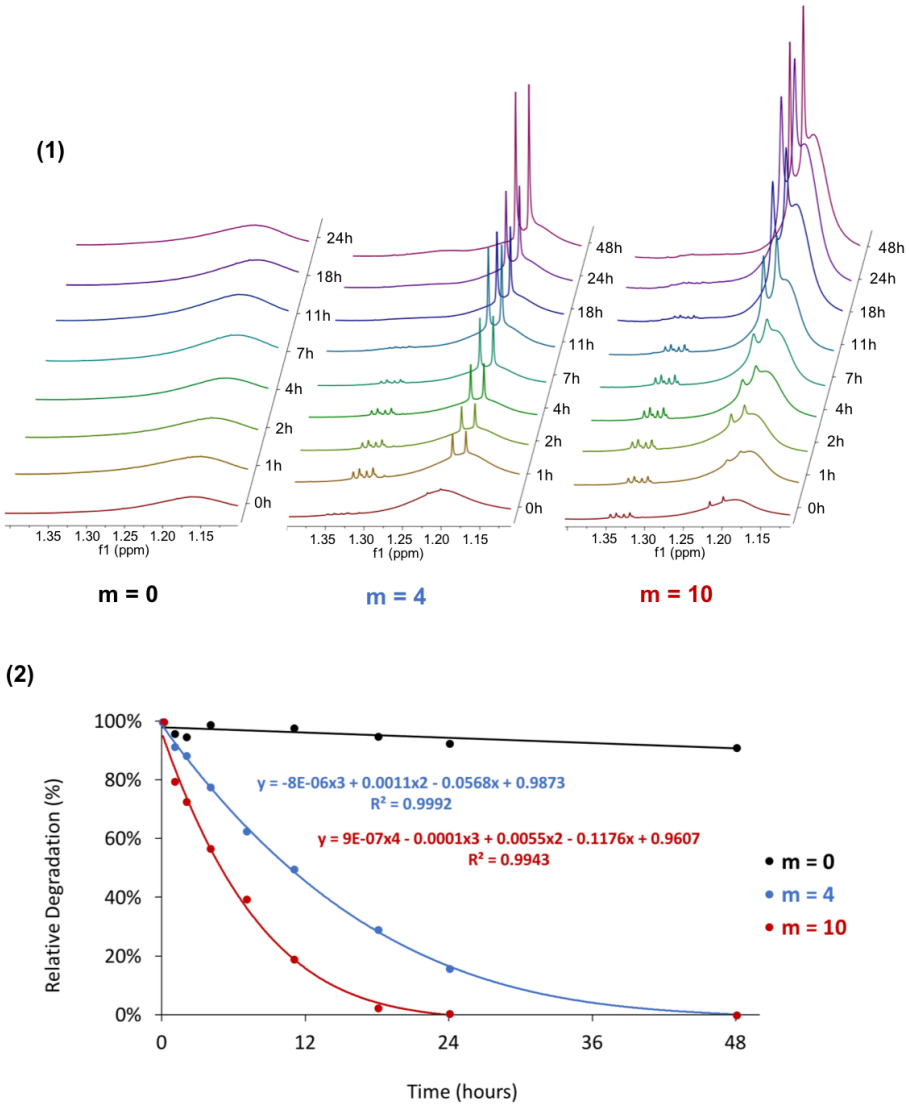

Figure 3.10 - NMR analysis of nanoparticle degradation by comparing the NMR spectra of m = 0, m = 4, m = 10 nanoparticles in accelerated degradation conditions as a function of time (1), and plotting the relative degradation as a function of time by integration of the peaks between 1.55 and 0.5 ppm

3.5 Protein Loading in the Nanoparticles

The experimental results of trypsin loading into the P(MMA-co-MAA) nanoparticles showed a high degree of variability between runs (**Figure 3.11**). Indeed, several loading conditions showed high degrees of loading such as "--++", "000A", and "+-++" with loading efficiencies of over 80%. In addition, certain runs showed very low protein loading such as "-+--" and "A000" which presented loading efficiencies of around 30% and 10%, respectively.

Inputting this experimental data in the JMP software, information regarding the relative influences of different loading variables and the ability to develop a predictive model based on the experimental data was obtained. As shown in **Figure 3.12.1**, the model developed by JMP has a high ability to accurately predict protein loading efficiency, with a predictive power p-value of less than 0.0001. In addition, the software identified the loading variables which have the most significant effect on nanoparticle protein loading efficiency (**Figure 3.12.2**.) The factors with the most influence were found to be: the square of the incubation time, the protein:polymer wt% ratios, the ionic strength of the buffer, and the square of the loading buffer pH.

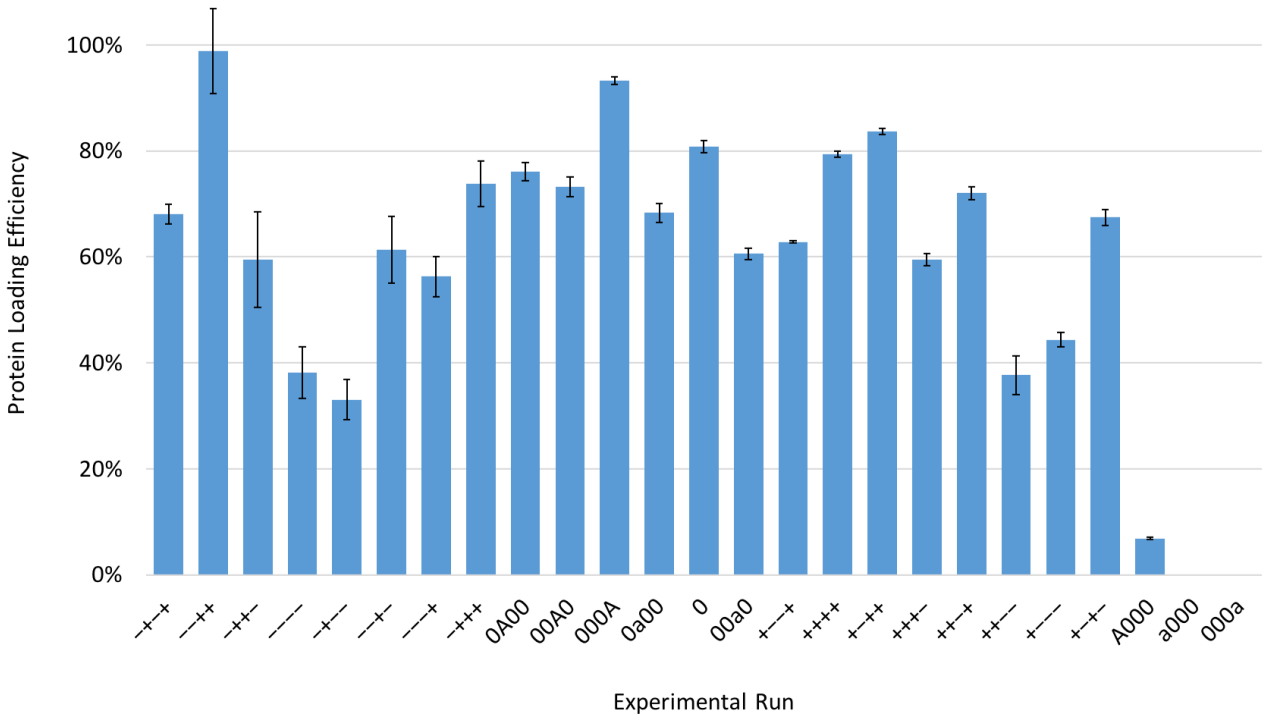

Figure 3.11 – Experimentally obtained protein loading efficiencies for the different loading conditions as defined in Appendix C

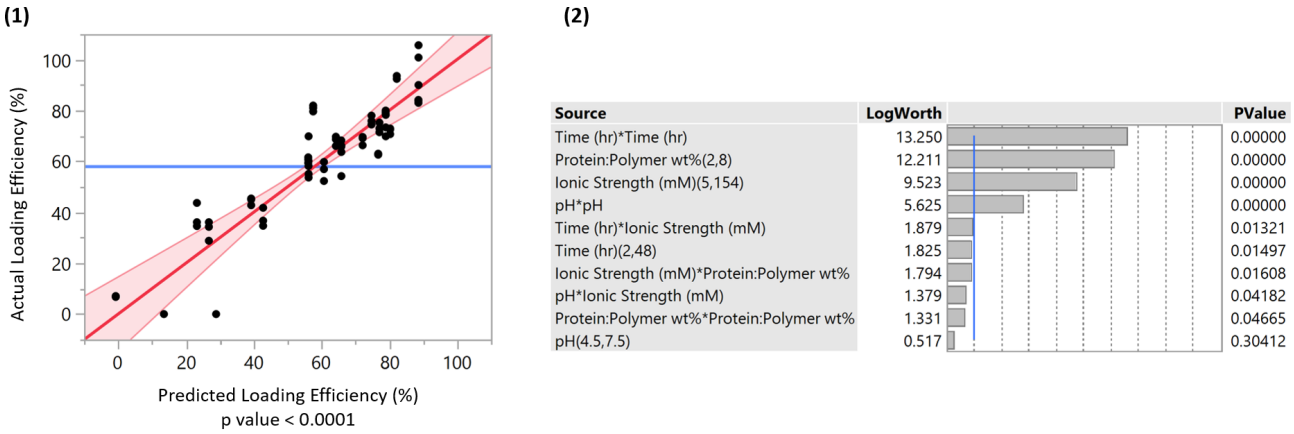

Figure 3.12 - (1) Comparison of the actual loading efficiency and the model predicted loading efficiency and (2) the effect summary of the various loading variables where p values < 0.05 correspond to a statistically significant effect on the loading protein loading efficiency

In addition, the JMP analysis provided the level for each loading variable to independently maximize protein loading efficiency (**Figure 3.13**). It is predicted that a loading time of 24.8 h can lead to maximum loading, as well as a pH of 4.5, an ionic strength of 154 mM and a protein to polymer ratio of 8 wt%.

The interactions between the different variables considered are described in **Figure 3.14**. These contour plots reveal the importance of taking into account these 2-factor interactions since the maximized values as defined in **Figure 3.13** do not lead to maximum loading at all levels of the other variables. For example, while the protein to polymer ratio which leads to the highest loading efficiency is 8 wt%, these high efficiencies are achieved when incubating for between 20 and 45 h, in buffers above 110 mM and at pH below 4.7 or above 7.2. However, 8 wt% protein:polymer achieves little to no loading if carried out in buffers below 80 mM, at pH around 6 or for incubation times higher than 50 h.

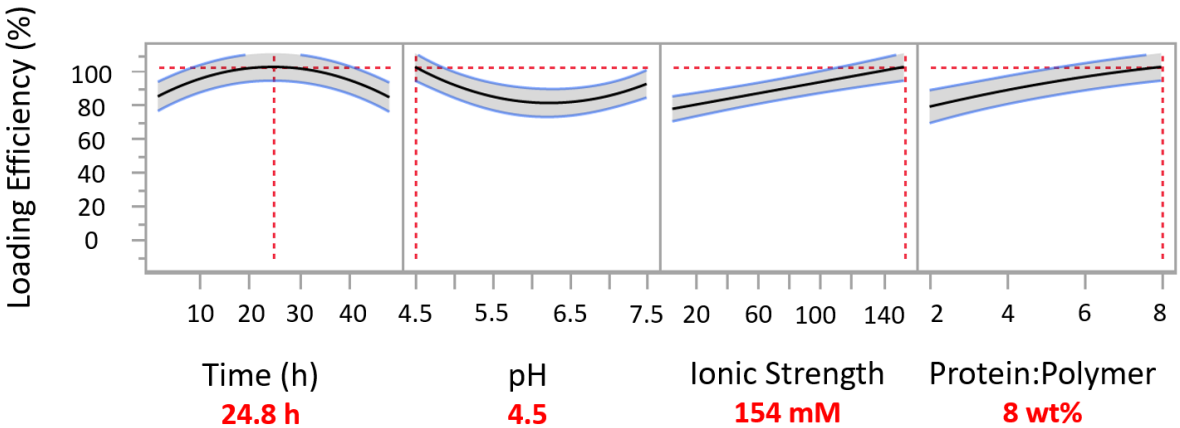

Figure 3.13 - Prediction profiler to maximize loading efficiency for each tested loading condition variable

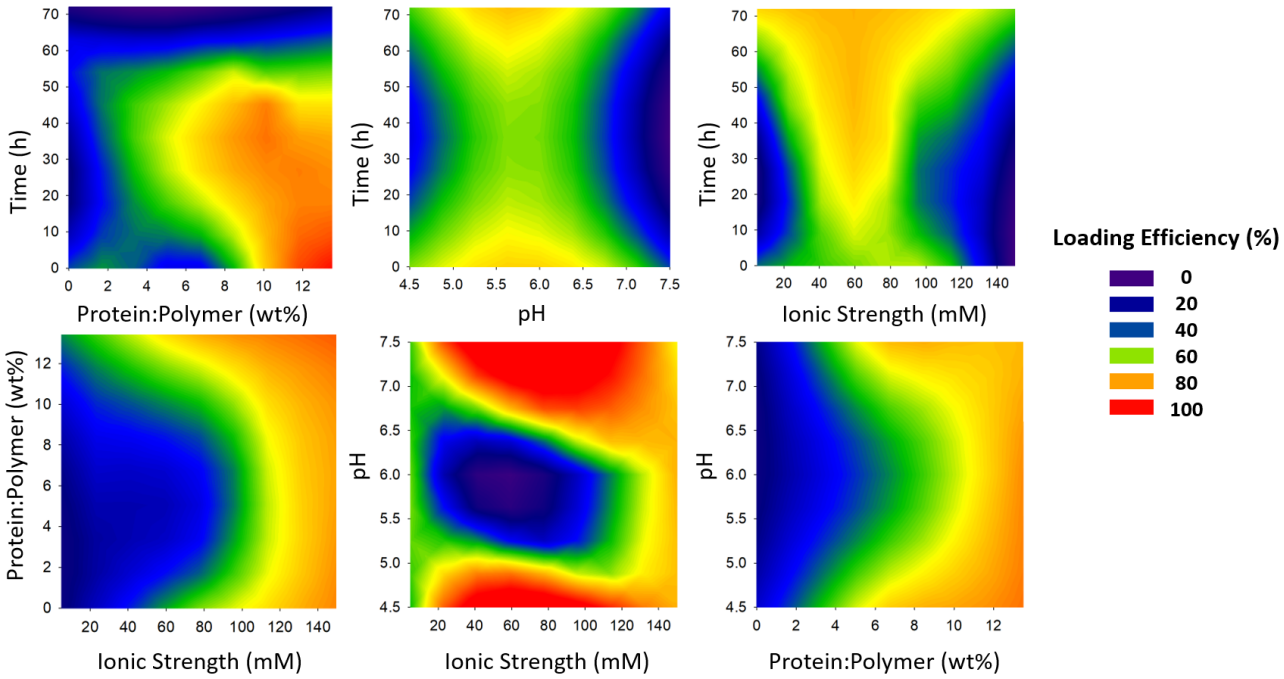

Figure 3.14 - Contour plots obtained from the protein loading analysis and taking into account 2-factor interactions, red areas indicate conditions which lead to maximum loading efficiency as predicted by the model

3.6 Immobilization of Nanoparticles within the Scaffold

Fluorescent images obtained immediately after loading show a high fluorescent intensity for all three systems, indicating the presence of protein (in blue) and particles (in red) within the bulk of the scaffolds (**Figure 3.15**.) After 30 minutes of incubation and 5 washes in phosphate buffered saline, a significant reduction in the amount of blue is observed, suggesting that within 30 minutes a large portion of the protein has diffused out of the scaffold. Similarly, a reduction in the amount of red is observed for the unbound particles, but the intensity remains relatively constant for the covalently bound particles. The fluorescent intensity of both the unbound protein and unbound particles continues to decrease over time, with no detectable presence in either system after 4 weeks. The covalently bound particle system, however, continues to show similar intensities across the different time points.

Finally, it was shown that the incorporation of covalently bound nanoparticles within the scaffold bulk does not have a significant effect on the scaffold mechanical properties, as shown in **Figure 3.16**. While a slight increase in storage modulus and decrease in loss modulus is observed for increasing amounts of nanoparticles within the scaffold, these changes remain within the margins of error.

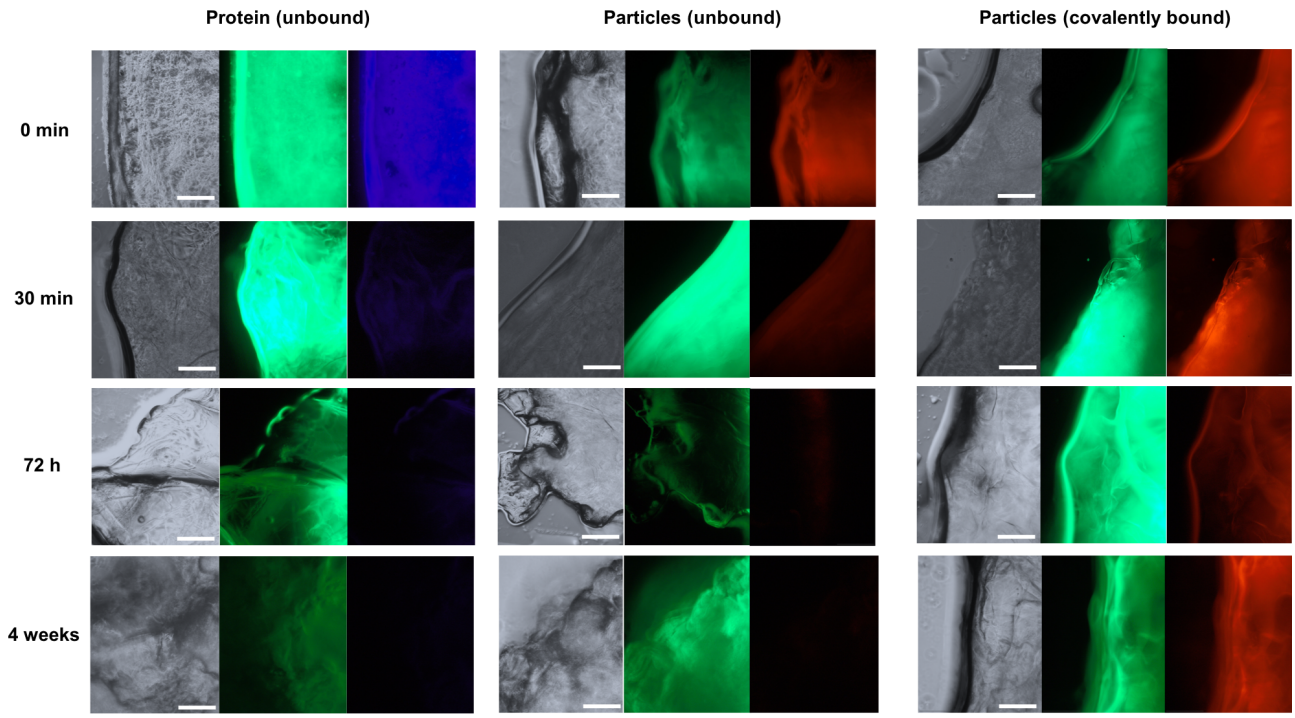

Figure 3.15 - Fluorescent imaging of FITC-labelled chitosan scaffolds (green) incorporated with unbound DAPI-labelled trypsin (blue, column 1), unbound Tamra cadaverine-labelled nanoparticles (red, column 2), and covalently bound Tamra cadaverine-labelled nanoparticles (red, column 3). Images were taken for each system immediately after loading and after 30 minutes, 72 hours, and 4 weeks of incubation. Scale bars: 60 µm

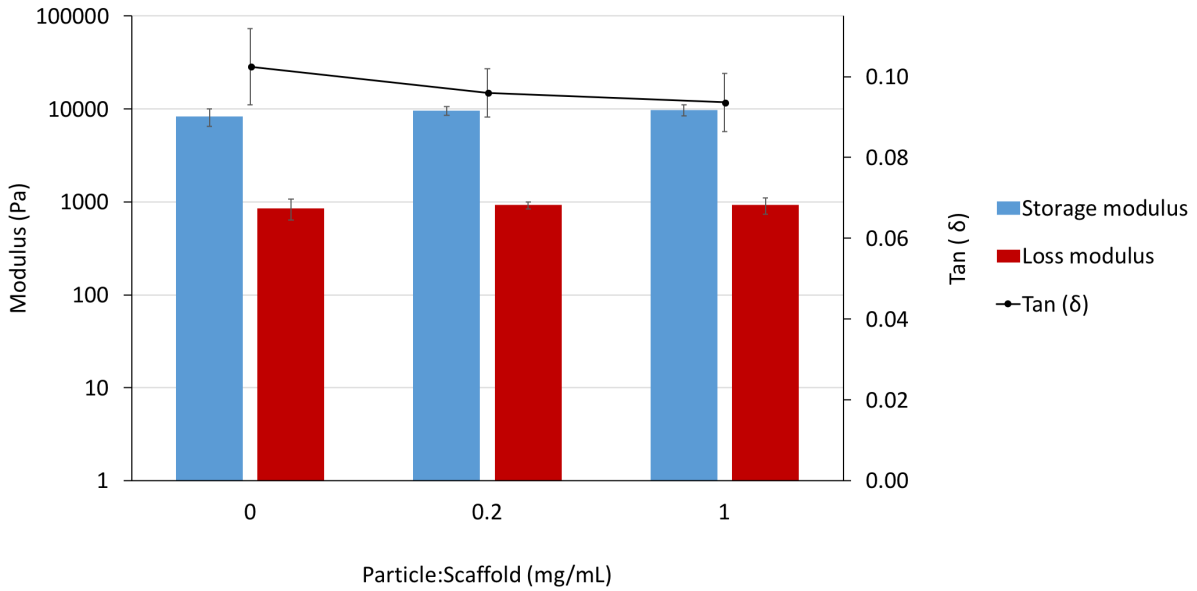

Figure 3.16 - Dynamic mechanical properties of two-phase scaffold-nanoparticle system with increasing ratios of particle mass to scaffold volume

3.7 In vitro Cytotcompatibilty Studies

3.7.1 In vitro Behavior of HUVECs in the Presence of Degradable Nanoparticles

MTS and LDH assays of HUVECs in the presence of both non-degraded and degraded particles show that the P(MMA-co-MAA) nanoparticles do not have significant cytotoxic effects on the cells. For the LDH assay, a value of 80% relative proliferation was considered to be the acceptable threshold value to indicate cellular compatibility. The results of the LDH membrane integrity assays for both the non-degraded and degraded particles indicate that cell viability values remain above 90% relative to the media control for concentrations up to 0.2 mg/mL (**Figure 3.17.B** and **Figure 3.18.B**.) The relative cell viability decreases for nanoparticle concentrations of 1 mg/mL but remain above 80% for both 24 hour and 48-hour exposure times.

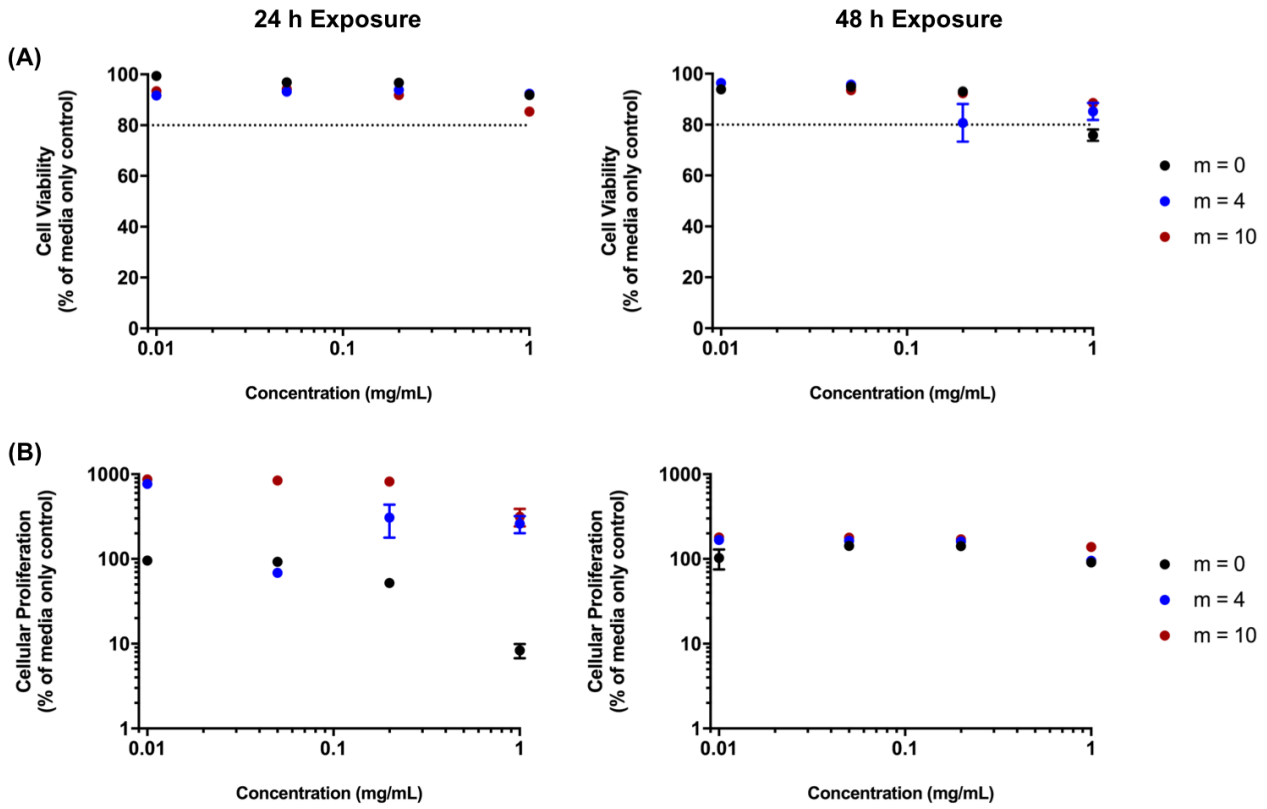

Figure 3.17 – Evaluation of cytocompatibility of non-degraded P(MMA-co-MAA) nanoparticles. (A) Cytocompatibility of HUVEC cells using an LDH cell membrane integrity assay after 24 h (left) and 48 h exposure (right). (B) Cytocompatibility of HUVEC cells using an MTS cellular proliferation assay after 24 h (left) and 48 h exposure (right).

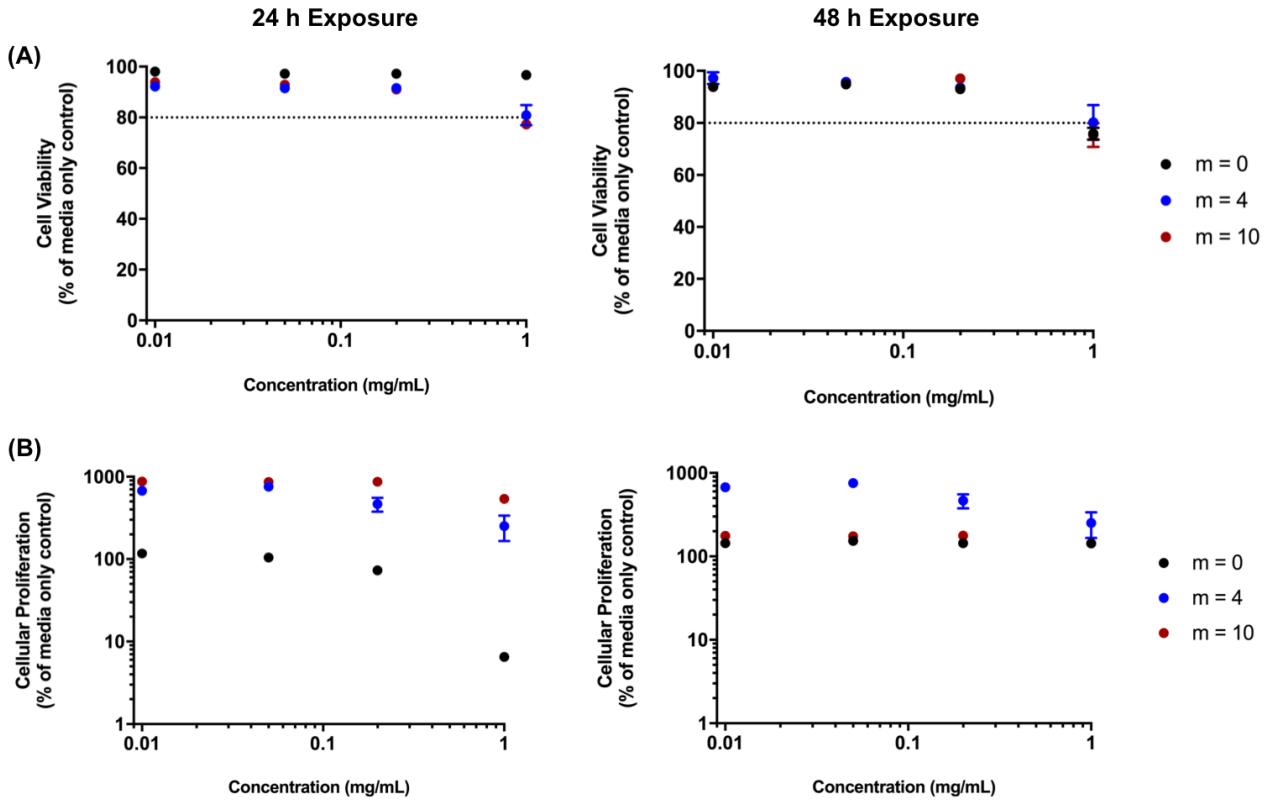

Figure 3.18 - Evaluation of cytocompatibility of degraded P(MMA-co-MAA) nanoparticles. (A) Cytocompatibility of HUVEC cells using an LDH cell membrane integrity assay after 24 h (left) and 48 h exposure (right). (B) Cytocompatibility of HUVEC cells using an MTS cellular proliferation assay after 24 h (left) and 48 h exposure (right).

Results of the cellular proliferation assay indicate that the non-degradable P(MMA-co-MAA) nanoparticles (m = 0) exhibit a concentration-dependent effect on cellular proliferation after 24 hours exposure, with cellular proliferation remaining above 80% relative to the media control for concentrations below 0.2 mg/mL but decreasing to around 10% for concentrations of 1 mg/mL (**Figure 3.17.A** and **Figure 3.18**.**A**).

This concentration-dependent behavior is also observed for the m = 4 and m = 10 degradable particles; however, the proliferation values are significantly higher than that of the media control with up to 700% for the m = 4 nanoparticles and 900% for the m = 10 nanoparticles in both the non-degraded and degraded state. This effect is less pronounced after 48 hours of exposure to the non-degraded nanoparticles, with proliferation values remaining around 200% for all nanoparticles at all concentrations. Notably, after 48 hours of exposure, the m = 0 nanoparticles no longer exhibit the concentration-dependent effect, with proliferation values of around 150% up to concentrations of 1 mg/mL. In addition, after 48 hours of exposure, the increased proliferation effect is less pronounced for the degraded m = 4 and m = 10 nanoparticles when compared to the 24-hour exposure.

3.7.2 In vitro Behavior of HUVECs in the Presence of Chitosan Scaffolds

The results of cellular proliferation and cell viability assays for HUVECs in the presence of 2 wt% chitosan scaffolds with and without covalently bound nanoparticles indicate that the scaffold systems do not have a toxic effect on cells (**Figure 3.19**.) After both 24 and 48 hours of exposure, both the scaffold and scaffold with nanoparticles systems result in cell viabilities of above 95% relative to the media control, indicating that the system components do not result in cell lysis after 48 hours.

Further, after 24 hours of exposure to both the scaffold and the scaffold with covalently bound nanoparticles, the cells exhibit relative cellular proliferation of up to 800% when compared to the media control. This effect, while less significant, is still observed after 48 hours of exposure to the scaffold systems, with proliferation values up to 150%.

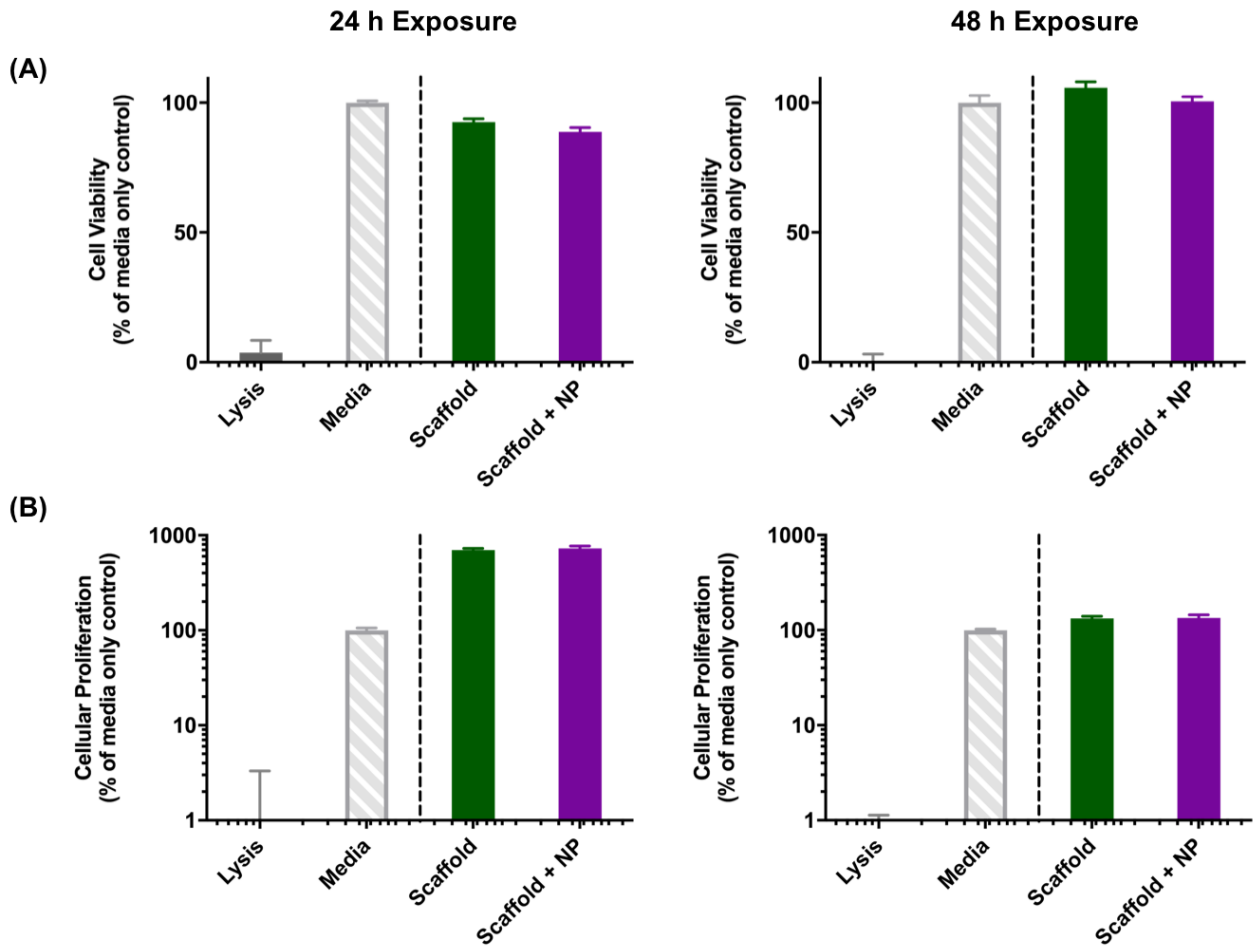

Figure 3.19 - Evaluation of cytocompatibility of 2 wt% chitosan scaffolds with and without bound P(MMA-co-MAA) nanoparticles. (A) Cytocompatibility of HUVEC cells using an LDH cell membrane integrity assay after 24 h (left) and 48 h exposure (right). (B) Cytocompatibility of HUVEC cells using an MTS cellular proliferation assay after 24 h (left) and 48 h exposure (right).

4 Discussion

4.1 Chitosan Scaffolds for Bone Tissue Engineering Applications

The mechanical properties of bone tissue engineering scaffolds are considered to be an essential characteristic to promote the osteogenic behavior of the material. Typical values of the compressive strength of cancellous bone are between 2 and 12 MPa while elastic modulus values range between 0.1 and 5 GPa [32]. In addition, the dynamic mechanical properties of cancellous bone have been found to be 800 kPa for the storage modulus, and 52 kPa for the loss modulus [33,34].

In general, natural polymers are highly attractive materials for bone tissue engineering scaffold applications due to their abundance in nature, inherent biocompatibility, and biodegradability. In addition, chitosan is particularly attractive as it presents mucoadhesive and antibacterial properties and has been shown to be osteoconductive [35]. A further advantage of chitosan in the proposed two-phase system is the presence of reactive primary amines along the polymer backbone which can be used for the immobilization of nanocarriers with reactive carboxyl groups via carbodiimide crosslinker chemistry. However, a key limitation in the use of natural polymers in general and chitosan in particular are their low mechanical strength though methods have been developed to fabricate high-strength natural-polymer based scaffold systems. Often these systems rely on the fabrication of natural polymer-based composites in combination with ceramics or synthetic polymers [36]. More recently, however, methods have been developed in order to fabricate high-strength pristine natural polymer-based systems [37].

In this work, scaffolds were fabricated by lyophilization of the chitosan solutions, referred to on the literature most often as the “freeze-drying method” [20]. This method is of particular interest in the fabrication of scaffold for bone tissue engineering as it leads to the formation of highly porous scaffolds with both large-scale pores and interconnected porosity. The observed pore size of around 300 μm has been considered optimal for bone tissue engineering applications [38,39]. In addition, the presence of larger-scale macropores was observed. This range in pore size could present further advantages for the regeneration of bone tissue, as it has been demonstrated that a hierarchical structure with multi-scale porosity can lead to higher osteoconductivity than systems with a uniform pore size [40].

The fabrication of bone tissue engineering scaffolds often leads to a trade-off between interconnected porosity and sufficient mechanical properties, since an increase in porosity and pore size can result in

a loss of mechanical integrity. The lyophilization method used in the present work led to the fabrication of scaffolds with a storage modulus of around 8.5 kPa. Wang and Stegemann developed crosslinked chitosan/collagen hydrogels for bone tissue engineering applications with a storage modulus of up to 0.35 kPa [41]. Similarly, Jin et al. developed an injectable chitosan-based scaffold with a storage modulus of up to 0.5 kPa in physiological conditions [42]. Therefore, when comparing the present system to existing systems in the literature, it is concluded that the freeze-drying system is a promising method to fabricate higher strength hydrated natural polymer networks.

In addition, the SEM images reveal a certain level of anisotropy in the fabricated scaffold as a result of pore orientation. This characteristic has been found to be desirable in the design of bone scaffolds since bone is primarily loaded anisotropically in the body [7]. Further, this characteristic is especially desirable for the regeneration of cancellous bone tissue which itself is an anisotropic material with viscoelastic mechanical behavior [43].

4.2 Nanoparticles with Tunable Degradation Rates

In the literature, nanoparticle-based approaches for growth factor delivery are considered to be a promising method to achieve sustained release profiles and promote tissue regeneration [44]. In this work, P(MMA-co-MAA) nanoparticles were successfully synthesized using a PEGDMA crosslinker. The observed negative surface charges of the particles (**Figure 3.3.2**) confirm the successful incorporation of methacrylic acid. In addition, the presence of these charges confirms the incorporation of PEGDMA as a crosslinker in the bulk of the particle rather than as a PEG coating on the surface of the particles. Indeed, PEG is often incorporated onto the surface of nanoparticles in order to reduce charge-based interactions with proteins and increase circulation time, imparting so-called “stealth” behavior [45].

Many nanoparticle-based approaches for the delivery of growth factors rely on nanoparticle degradation-mediated release of the payload to achieve desirable sustained release profiles [16]. One method to impart degradability to a hydrogel system is through the introduction of labile bonds on the crosslinker [46]. In fact, the use of degradable crosslinkers for the release of growth factors such as BMP-2 has been explored before in different systems. For example, Tellier et al. developed heparin-based microparticles for the release of BMP-2 using a hydrolytically degradable crosslinker and showed a slow and sustained release of BMP-2 [47]. Similarly, Li et al. developed crosslinked micelles for the controlled release of a hydrophobic payload based on a similar PLA/PEG block-copolymer as

used in the present system [48]. Although in the system developed by Li et al. the PLA/PEG macromolecule is used not as a crosslinker but rather as the bulk nanoparticle material, it was shown that changing the length of the PLA segments allowed for control of the payload release profile, as is hypothesized in the present design.

As was similarly demonstrated by Diederich et al., the degradation rate of a PEG-based hydrogel can be increased by increasing the number of incorporated lactic acid units along the PEG chain [26]. In this work, these degradable MA-PLA-b-PEG-b-PLA-MA macromolecules were synthesized in order to subsequently be incorporated as crosslinkers into the P(MMA-co-MAA) nanoparticle synthesis scheme. As shown in **Figure 3.5**, the degradable nanoparticles have relatively constant hydrodynamic diameters despite being synthesized using different crosslinkers. This can be attributed to the fact that the length of the PEG chain was adapted for each custom crosslinker synthesis scheme such that the final crosslinkers would have lengths comparable to that of PEGDMA MW=600. In addition, a wider distribution of hydrodynamic diameters for the custom crosslinked nanoparticles was observed and can be explained by a wider distribution in the lengths of the custom crosslinker chains. Indeed, the values obtained by integration of the NMR spectra (**Figure 3.4**) provide only an average value of the lactic acid unit incorporation. However, it is likely that the number of lactic acid units incorporated may follow a wide distribution, which would lead to a wide distribution of crosslinker chain length and therefore nanoparticle hydrodynamic diameter.

The analysis of different makers of nanoparticle degradation provides evidence that the custom macromolecules which were synthesized and incorporated as crosslinkers in the nanoparticle fabrication scheme impart a certain degree of degradability to the nanoparticles. In addition, a comparison between nanoparticles fabricated with varying degrees of lactic acid unit incorporation shows that the developed system presents a degree of tunability, with m = 10 nanoparticles presenting a higher rate of degradation than the m = 4 nanoparticles. This is observed by the difference in rate of the count rate decrease as a function of time, the amount of visible intact particles via TEM, and the rate of degradation via quantitative NMR analysis. This observation is in line with the hypothesis that increasing the number of degradable bonds along the crosslinker is a viable method to tune the degradability of nanoparticles [46].

This tunability of the nanoparticle degradation can be harnessed in order to optimize the system for the delivery of particular growth factors. It is known that the release kinetics of particulate carriers are highly determined by the rate of degradation of the carrier in question [16]. Therefore, fabricating a

nanocarrier which degrades more or less rapidly can be adapted for the delivery of growth factors which are relevant at either early or late stages of tissue regeneration. For BMP-2 and bone regeneration specifically, it is known that the regeneration of bone tissue is a highly dynamic process consisting of coordinated cellular responses over several weeks [49] with most systems in the literature seeking to optimize systems for the sustained delivery of BMP-2 for up to 4 weeks [50]. In this work, it was demonstrated that the m = 4 nanoparticles would be fully degraded after 6 weeks *in vivo*, whereas the m = 10 particles would fully degrade after 3 weeks *in vivo*, time scales which are relevant for bone tissue engineering applications.

The results of the *in vitro* studies indicate that the incorporation of custom degradable crosslinkers in the synthesis of P(MMA-co-MAA) nanoparticles does not result in cytotoxic effects on HUVECs up to concentrations of 1 mg/mL and 48 hours of exposure. In addition, cellular proliferation assay results show that in the presence of degraded nanoparticles, HUVECs exhibit up to a 9-fold increase in proliferation relative to the positive media control, behavior which is not observed for the non-degradable particles. This suggests a positive effect of the nanoparticle degradation byproducts on cell proliferation. As shown in **Figure 3.10**, NMR data confirms the appearance of lactic acid as a function of time as a result of nanoparticle degradation. In physiological conditions, lactic acid can dissociate into a lactate ion and a hydrogen ion and can thereby affect the metabolic function of the surrounding cells [51]. Specifically, Groussard et al. showed that lactate ions can have antioxidant effects by scavenging superoxide and hydroxyl radicals as well as limiting lipid peroxidation thereby protecting cells from oxidative damage [52]. Lampe et al. showed that an increase in lactic acid concentration up to 0.5 mg/mL resulted in a 100% increase in total DNA content relative to the control in fetal forebrain cells, which was attributed to a reduction in cellular redox state [51]. In addition, Beckert et al. showed that in HUVECs specifically, an increase in lactate can enhance VEGF production, resulting in an increase in cellular migration [53]. Therefore, the observed positive effect of degraded P(MMA-co-MAA) nanoparticles on HUVEC proliferation can be explained by the release of lactic acid and indicates the ability of the proposed system to promote angiogenesis, considered to be essential to successful bone regeneration [54].

Ultimately, the novelty of this system lies in the ability to adjust the number of lactic acid units along the crosslinker chains in order to achieve specific degradation times without significantly altering other key properties of the carrier system. In addition, the degradation of nanoparticles does not lead to cell lysis and rather can promote cell proliferation through the release of lactic acid byproducts.

4.3 Protein Loading Ability of P(MMA-co-MAA) Nanoparticles

The proposed system is designed to deliver growth factors relevant for bone tissue engineering in a controlled and sustained way. The synthesized nanoparticles were therefore designed to have high affinity for BMP-2 which is a high molecular weight, high isoelectric point, hydrophobic protein, and commonly used in bone tissue engineering applications. It should be noted that many studies use bovine serum albumin (BSA) as a model for BMP-2 [55,56]. However, BSA has a much higher molecular weight of around 66.5 kDa (when compared to 30 kDa for BMP-2) and a low isoelectric point of 4.7 (in contrast to 8.5 for BMP-2). Because both size and electrostatic interactions will greatly influence the partitioning of protein into the nanoparticles, trypsin with a molecular weight of 23.3 kDa and an isoelectric point of 10.1 was used as a more accurate model to understand the ability of the selected system to load growth factors such as BMP-2.

The results of the protein loading study point to the excellent ability of the synthesized P(MMA-co-MAA) nanoparticles to load the model protein. Indeed, loading efficiencies up to 100 % were observed for certain loading conditions. In addition, the experimental results pointed to the importance of choosing appropriate loading conditions since loading efficiencies ranged between 10% and 100% simply by changing certain loading variables. In fact, all four loading conditions were shown to have a significant effect on protein loading efficiency, with incubation time and pH having second order effects while protein to polymer ratio and buffer strength had first order effects.

The loading time can have an important effect on protein loading, since increased times increase the chances of protein uptake by the particles, but because the system can reach an equilibrium, extending loading for longer times could lead to reduced protein incorporation. This phenomenon was indeed observed, with a 24.8-hour incubation leading to maximum loading, and times above 48 hours leading to a significant loss of loading efficiency. It was also shown that higher values of protein: polymer ratios allow for improved loading, and that an ionic strength of 154 mM is desirable. This buffer strength corresponds to that at which proteins similar to BMP-2 are most stable. Interestingly, a pH of 4.5 was found to lead to the highest loading efficiency, which despite the aggregation of particles in low pH conditions can be explained by the high stability of protein in acidic environments.

Ultimately, this work demonstrates the excellent ability of the synthesized nanoparticles to load a model protein for BMP-2. This result reflects the importance of understanding protein properties and polymer selection in designing nanocarriers. In addition, a mathematical model was obtained to further understand the effects of loading variables on observed loading efficiency. It was found that all factors

had a statistically significant effect and can be optimized for the system in order to achieve maximum loading. Finally, a key advantage in the use of nanoparticles for growth factor delivery is the ability to tune the delivered dose in order to achieve the desired tissue response. Through understanding the protein loading efficiency of the nanoparticles, the amount of nanoparticles loaded into the scaffold carrier can be tuned in order to control the delivered dose to the site of injury.

4.4 Effect of Nanoparticle Immobilization on their Sustained Retention and Scaffold Properties

The majority of growth factor delivery systems explored in the literature rely on the adsorption of growth factors within the bulk of highly porous scaffolds [57,58]. These systems are most often associated with a rapid burst release of the incorporated protein which is considered to be a key limitation of this incorporation approach. This rapid burst release behavior can be explained by the highly porous nature of scaffolds used for bone tissue engineering applications which allows for growth factors with diameters of only several nanometers to easily diffuse through the pore network. However, this leads to a tradeoff since high porosities are considered to be necessary in the design of bone tissue engineering scaffolds and have been found to be essential to the vascularization of the newly forming bone [21,32,38]. Furthermore, the likelihood of a burst release profile is increased upon implantation of the scaffold into the body due to the highly dynamic physiological environment where fluid flow and diffusion can have a large impact on protein retention.

One common approach for the improved retention of growth factors within the scaffold bulk is through their encapsulation into nanoparticles [59,60]. This method has been shown to lead to improved release profiles, still presenting an initial burst release which is followed by a sustained release profile. However, the ratio of particle diameter to scaffold pore size remains extremely small, with most nanoparticle systems having a diameter of around 100 nm and pore sizes for bone tissue engineering scaffolds ranging from 200 to 500 μm. This difference suggests that nanoparticles may still easily diffuse out of the scaffold once implanted in the body and in contact with the dynamic fluid flow *in vivo*.

The system developed in this study aims to eliminate the potential of both protein and particles to diffuse rapidly out of the scaffold bulk through a novel approach: the covalent binding of particles to the scaffold backbone. While covalent binding approaches have previously been used for growth factor delivery applications, these previous systems rely on the covalent binding of growth factors themselves

to the scaffold backbone. However, this method poses concerns due to the high chance of negatively affecting protein bioactivity [17].

The results of the fluorescent imaging experiment suggest that common methods of growth factor and nanoparticle incorporation into scaffolds results in their rapid diffusion out of the scaffold bulk. Proteins in the scaffold were no longer visibly detectable after 72 hours and nanoparticles were fully removed after 4 weeks. In contrast, nanoparticles which were covalently bound to the scaffold were still present within the scaffold after 4 weeks. These results suggest that the diffusion of nanoparticles out of the scaffold carrier can present a significant limitation to current systems proposed in the literature. This phenomenon can explain the burst release of growth factor observed for such systems but can be reduced by the novel approach of covalently binding nanocarriers to the scaffold bulk. Furthermore, the retention of nanoparticles for multiple weeks reflects the potential of such systems to deliver essential growth factors such as BMP-2 which are desired to be present within bone regeneration sites for up to 4 weeks after injury [11].

The incorporation of nanoparticles within the scaffold bulk may also provide further advantages such as improved mechanical properties and structural hierarchy which can further promote the regeneration of bone tissue [60]. In the present work, no significant change in mechanical properties was detected for the incorporation of 0.2 and 1 mg/mL of covalently bound nanoparticles within the scaffold when compared to the control chitosan scaffold. However, this can be explained by the low concentrations of nanoparticles tested, and systems could be developed which incorporate unloaded nanoparticles as well as loaded nanoparticles to improve mechanical properties without affecting the delivered dose of growth factors.

Finally, *in vitro* studies evaluating the effect of chitosan scaffolds with and without covalently bound P(MMA-co-MAA) nanoparticles on HUVEC viability and proliferation indicate that the incorporation of nanoparticles within the chitosan scaffolds through covalent binding does not have a cytotoxic effect on HUVECs. In fact, *in vitro* results suggest that the 2 wt% chitosan scaffolds can lead to increased HUVEC proliferation in the first 48 hours of exposure when compared to a media control, and that this effect is not reduced by the incorporation of covalently bound nanoparticles. Chitosan has been identified as an excellent pro-angiogenic biomaterial and its use has also been explored in cardiovascular tissue engineering applications [61]. In fact, chitosan has been commonly incorporated into collagen-based tissue engineering systems in order to improve vascularization [62]. McBane et al. showed that the fabrication of a 10:1 collagen:chitosan hydrogel led to increased endothelial

progenitor cell viability and endothelial differentiation when compared to a pure collagen scaffold [63]. The pro-angiogenic characteristics of chitosan as demonstrated in the literature therefore explain the observed increase in HUVEC proliferation on the chitosan scaffolds when compared to the media controls. The non-cytotoxic and proliferative effect of the proposed two-phase scaffold-nanoparticle system therefore constitutes a promising approach to promote the regeneration of vascularized bone tissue.

5 Conclusions

The present work serves as a proof of concept for the development of a novel two-phase bone tissue engineering system, consisting of a porous chitosan scaffold that incorporates covalently bound, hydrolytically degradable nanoparticles with tunable degradation rates for loading and sustained release of proteins.

The results of this study show that P(MMA-co-MAA) nanoparticles designed to have high affinity for high isoelectric point, large molecular weight proteins such as BMP-2 can be fabricated in a simple and reproducible way via a one-pot UV-initiated emulsion polymerization scheme. In addition, this system was shown to be able to load a model protein for BMP-2 at efficiencies of up to 100% and loading conditions to maximize protein loading were identified.

Furthermore, a degradable crosslinker was custom-synthesized and incorporated into the P(MMA-co-MAA) nanoparticles to introduce varying degrees of degradability. Indeed, it was shown that by varying the number of hydrolytically degradable units along the crosslinker chain, the rate of degradation could be tuned to meet the desired protein release profile.

Finally, a novel method to prevent diffusion of nanoparticles out of the scaffold after implantation was proposed. It was shown that the covalent binding of particles to the scaffold backbone allows for the sustained retention of the carriers within the scaffold bulk over the relevant therapeutic timeframe.

Overall, this tunable platform can be developed for a variety of growth factor delivery applications. This system can potentially be adapted to achieve a controlled, sequential delivery of multiple growth factors by simply optimizing the degradation kinetics of the nanoparticles. In fact, sequential delivery systems have been identified as essential to the highly complex bone regeneration process and have the potential to for example simultaneously promote osteogenesis and angiogenesis for the formation of vascularized bone [64].

Ultimately, this work demonstrates that the incorporation of two-phase systems consisting of growth factor-loaded nanoparticles embedded into scaffolds have great promise, both by providing sustained release over a therapeutically relevant timeframe and the potential to sequentially deliver multiple growth factors.

References

1. Amini AR, Laurencin CT, Nukavarapu SP. Bone tissue engineering: Recent advances and challenges. *Crit Rev Biomed Eng* 2012;**40**:363–408.

2. Habibovic P. Strategic Directions in Osteoinduction and Biomimetics. *Tissue Eng Part A* 2017;**23**:1295–6.

3. Fröhlich M, Grayson WL, Wan LQ, Marolt D, Drobnic M, Vunjak-Novakovic G. Tissue Engineered Bone Grafts: Biological Requirements, Tissue Culture and Clinical Relevance. *Curr Stem Cell Res Ther* 2008;**3**:254–64.

4. Myeroff C, Archdeacon M. Autogenous bone graft: donor sites and techniques. *J Bone Joint Surg Am* 2011;**93**:2227–36.

5. Calori GM, Colombo M, Mazza EL, Mazzola S, Malagoli E, Mineo GV. Incidence of donor site morbidity following harvesting from iliac crest or RIA graft. *Injury* 2014;**45 Suppl 6**:S116-120.

6. Dimitriou R, Mataliotakis GI, Angoules AG, Kanakaris NK, Giannoudis PV. Complications following autologous bone graft harvesting from the iliac crest and using the RIA: a systematic review. *Injury* 2011;**42 Suppl 2**:S3-15.

7. Bose S, Roy M, Bandyopadhyay A. Recent advances in bone tissue engineering scaffolds. *Trends Biotechnol Oxf* 2012;**30**:546–54.

8. Oryan A, Alidadi S, Moshiri A, Maffulli N. Bone regenerative medicine: classic options, novel strategies, and future directions. *J Orthop Surg* 2014;**9**:18.

9. Saravanan S, Leena RS, Selvamurugan N. Chitosan based biocomposite scaffolds for bone tissue engineering. *Int J Biol Macromol* 2016;**93**:1354–65.

10. Balagangadharan K, Dhivya S, Selvamurugan N. Chitosan based nanofibers in bone tissue engineering. *Int J Biol Macromol* 2017;**104**:1372–82.

11. Hankenson KD, Gagne K, Shaughnessy M. Extracellular signaling molecules to promote fracture healing and bone regeneration. *Adv Drug Deliv Rev* 2015;**94**:3–12.

12. Chen D, Zhao M, Mundy GR. Bone morphogenetic proteins. *Growth Factors Chur Switz* 2004;**22**:233–41.

13. El Bialy I, Jiskoot W, Reza Nejadnik M. Formulation, Delivery and Stability of Bone Morphogenetic Proteins for Effective Bone Regeneration. *Pharm Res* 2017;**34**:1152–70.

14. Azevedo HS, Pashkuleva I. Biomimetic supramolecular designs for the controlled release of growth factors in bone regeneration. *Adv Drug Deliv Rev* 2015;**94**:63–76.

15. Agrawal V, Sinha M. A review on carrier systems for bone morphogenetic protein-2. *J Biomed Mater Res B Appl Biomater* 2017;**105**:904–25.

16. Vo TN, Kasper FK, Mikos AG. Strategies for controlled delivery of growth factors and cells for bone regeneration. *Adv Drug Deliv Rev* 2012;**64**:1292–309.

17. Di Luca A, Klein-Gunnewiek M, Vancso JG, van Blitterswijk CA, Benetti EM, Moroni L. Covalent Binding of Bone Morphogenetic Protein-2 and Transforming Growth Factor-β3 to 3D Plotted Scaffolds for Osteochondral Tissue Regeneration. *Biotechnol J* 2017;**12**, DOI: 10.1002/biot.201700072.

18. Bessa PC, Machado R, Nürnberger S, Dopler D, Banerjee A, Cunha AM, Rodríguez-Cabello JC, Redl H, van Griensven M, Reis RL, Casal M. Thermoresponsive self-assembled elastin-based nanoparticles for delivery of BMPs. *J Controlled Release* 2010;**142**:312–8.

19. Subbiah R, Hwang MP, Van SY, Do SH, Park H, Lee K, Kim SH, Yun K, Park K. Osteogenic/Angiogenic Dual Growth Factor Delivery Microcapsules for Regeneration of Vascularized Bone Tissue. *Adv Healthc Mater* 2015;**4**:1982–92.

20. Beck SC, Jiang T, Nair LS, Laurencin CT. 2 - Chitosan for bone and cartilage regenerative engineering. In: Jennings JA, Bumgardner JD (eds.). *Chitosan Based Biomaterials Volume 2*. Woodhead Publishing, 2017, 33–72.

21. Annabi N, Nichol JW, Zhong X, Ji C, Koshy S, Khademhosseini A, Dehghani F. Controlling the porosity and microarchitecture of hydrogels for tissue engineering. *Tissue Eng Part B Rev* 2010;**16**:371–83.

22. Han J, Ma G, Nie J. A facile fabrication of porous PMMA as a potential bone substitute. *Mater Sci Eng C* 2011;**31**:1278–84.

23. King WJ, Krebsbach PH. Growth factor delivery: How surface interactions modulate release in vitro and in vivo. *Adv Drug Deliv Rev* 2012;**64**:1239–56.

24. Fisher OZ, Peppas NA. Polybasic Nanomatrices Prepared by UV-Initiated Photopolymerization. *Macromolecules* 2009;**42**:3391–8.

25. Sawhney AS, Pathak CP, Hubbell JA. Bioerodible hydrogels based on photopolymerized poly(ethylene glycol)-co-poly(.alpha.-hydroxy acid) diacrylate macromers. *Macromolecules* 1993;**26**:581–7.

26. Diederich VEG, Villiger T, Storti G, Lattuada M. Modeling of the Degradation of Poly(ethylene glycol)-co-(lactic acid)-dimethacrylate Hydrogels. *Macromolecules* 2017;**50**:5527–38.

27. Browning MB, Cereceres SN, Luong PT, Cosgriff-Hernandez EM. Determination of the in vivo degradation mechanism of PEGDA hydrogels. *J Biomed Mater Res A* 2014;**102**:4244–51.

28. Choi JW, Jeong WS, Yang SJ, Park EJ, Oh TS, Koh KS. Appropriate and Effective Dosage of BMP-2 for the Ideal Regeneration of Calvarial Bone Defects in Beagles. *Plast Reconstr Surg* 2016;**138**:64e-72e.

29. Ben-David D, Srouji S, Shapira-Schweitzer K, Kossover O, Ivanir E, Kuhn G, Müller R, Seliktar D, Livne E. Low dose BMP-2 treatment for bone repair using a PEGylated fibrinogen hydrogel matrix. *Biomaterials* 2013;**34**:2902–10.

30. Zara JN, Siu RK, Zhang X, Shen J, Ngo R, Lee M, Li W, Chiang M, Chung J, Kwak J, Wu BM, Ting K, Soo C. High doses of bone morphogenetic protein 2 induce structurally abnormal bone and inflammation in vivo. *Tissue Eng Part A* 2011;**17**:1389–99.

31. Samarajeewa S, Shrestha R, Li Y, Wooley KL. Degradability of Poly(Lactic Acid)-Containing Nanoparticles: Enzymatic Access through a Cross-Linked Shell Barrier. *J Am Chem Soc* 2012;**134**:1235–42.

32. Wu S, Liu X, Yeung KWK, Liu C, Yang X. Biomimetic porous scaffolds for bone tissue engineering. *Mater Sci Eng R Rep* 2014;**80**:1–36.

33. Yilgor P, Sousa RA, Reis RL, Hasirci N, Hasirci V. 3D Plotted PCL Scaffolds for Stem Cell Based Bone Tissue Engineering. *Macromol Symp* 2008;**269**:92–9.

34. Töyräs J, Nieminen MT, Kröger H, Jurvelin JS. Bone mineral density, ultrasound velocity, and broadband attenuation predict mechanical properties of trabecular bone differently. *Bone* 2002;**31**:503–7.

35. Venkatesan J, Anil S, Kim S-K, Shim MS. Chitosan as a vehicle for growth factor delivery: Various preparations and their applications in bone tissue regeneration. *Int J Biol Macromol* 2017;**104**:1383–97.

36. Rao SH, Harini B, Shadamarshan RPK, Balagangadharan K, Selvamurugan N. Natural and synthetic polymers/bioceramics/bioactive compounds-mediated cell signaling in bone tissue engineering. *Int J Biol Macromol* 2017, DOI: 10.1016/j.ijbiomac.2017.09.029.

37. Jana S, Florczyk SJ, Leung M, Zhang M. High-strength pristine porous chitosan scaffolds for tissue engineering. *J Mater Chem* 2012;**22**:6291–9.

38. Karageorgiou V, Kaplan D. Porosity of 3D biomaterial scaffolds and osteogenesis. *Biomaterials* 2005;**26**:5474–91.

39. Loh QL, Choong C. Three-Dimensional Scaffolds for Tissue Engineering Applications: Role of Porosity and Pore Size. *Tissue Eng Part B Rev* 2013;**19**:485–502.

40. Woodard JR, Hilldore AJ, Lan SK, Park CJ, Morgan AW, Eurell JAC, Clark SG, Wheeler MB, Jamison RD, Wagoner Johnson AJ. The mechanical properties and osteoconductivity of hydroxyapatite bone scaffolds with multi-scale porosity. *Biomaterials* 2007;**28**:45–54.

41. Wang L, Stegemann JP. Glyoxal crosslinking of cell-seeded chitosan/collagen hydrogels for bone regeneration. *Acta Biomater* 2011;**7**:2410–7.

42. Jin R, Moreira Teixeira LS, Dijkstra PJ, Karperien M, van Blitterswijk CA, Zhong ZY, Feijen J. Injectable chitosan-based hydrogels for cartilage tissue engineering. *Biomaterials* 2009;**30**:2544–51.

43. Mathieu LM, Mueller TL, Bourban P-E, Pioletti DP, Müller R, Månson J-AE. Architecture and properties of anisotropic polymer composite scaffolds for bone tissue engineering. *Biomaterials* 2006;**27**:905–16.

44. Corona-Gomez J, Chen X, Yang Q. Effect of Nanoparticle Incorporation and Surface Coating on Mechanical Properties of Bone Scaffolds: A Brief Review. *J Funct Biomater* 2016;**7**, DOI: 10.3390/jfb7030018.

45. Jokerst JV, Lobovkina T, Zare RN, Gambhir SS. Nanoparticle PEGylation for imaging and therapy. *Nanomed* 2011;**6**:715–28.

46. Hennink WE, van Nostrum CF. Novel crosslinking methods to design hydrogels. *Adv Drug Deliv Rev* 2012;**64**:223–36.

47. Tellier LE, Miller T, McDevitt TC, Temenoff JS. Hydrolysis and Sulfation Pattern Effects on Release of Bioactive Bone Morphogenetic Protein-2 from Heparin-Based Microparticles. *J Mater Chem B Mater Biol Med* 2015;**3**:8001–9.

48. Li J, Guo S, Wang M, Ye L, Yao F. Poly(lactic acid)/poly(ethylene glycol) block copolymer based shell or core cross-linked micelles for controlled release of hydrophobic drug. *RSC Adv* 2015;**5**:19484–92.

49. Hettiaratchi MH, Rouse T, Chou C, Krishnan L, Stevens HY, Li M-TA, McDevitt TC, Guldberg RE. Enhanced in vivo retention of low dose BMP-2 via heparin microparticle delivery does not accelerate bone healing in a critically sized femoral defect. *Acta Biomater* 2017;**59**:21–32.

50. Krishnan L, Priddy LB, Esancy C, Klosterhoff BS, Stevens HY, Tran L, Guldberg RE. Delivery vehicle effects on bone regeneration and heterotopic ossification induced by high dose BMP-2. *Acta Biomater* 2017;**49**:101–12.

51. Lampe KJ, Namba RM, Silverman TR, Bjugstad KB, Mahoney MJ. Impact of Lactic Acid on Cell Proliferation and Free Radical Induced Cell Death in Monolayer Cultures of Neural Precursor Cells. *Biotechnol Bioeng* 2009;**103**:1214–23.

52. Groussard C, Morel I, Chevanne M, Monnier M, Cillard J, Delamarche A. Free radical scavenging and antioxidant effects of lactate ion: an in vitro study. *J Appl Physiol Bethesda Md 1985* 2000;**89**:169–75.

53. Beckert S, Farrahi F, Aslam RS, Scheuenstuhl H, Königsrainer A, Hussain MZ, Hunt TK. Lactate stimulates endothelial cell migration. *Wound Repair Regen Off Publ Wound Heal Soc Eur Tissue Repair Soc* 2006;**14**:321–4.

54. Hankenson KD, Dishowitz M, Gray C, Schenker M. Angiogenesis in bone regeneration. *Injury* 2011;**42**:556–61.

55. Yilgor P, Tuzlakoglu K, Reis RL, Hasirci N, Hasirci V. Incorporation of a sequential BMP-2/BMP-7 delivery system into chitosan-based scaffolds for bone tissue engineering. *Biomaterials* 2009;**30**:3551–9.

56. Liu T, Wu G, Zheng Y, Wismeijer D, Everts V, Liu Y. Cell-mediated BMP-2 release from a novel dual-drug delivery system promotes bone formation. *Clin Oral Implants Res* 2014;**25**:1412–21.

57. Ferrand A, Eap S, Richert L, Lemoine S, Kalaskar D, Demoustier-Champagne S, Atmani H, Mély Y, Fioretti F, Schlatter G, Kuhn L, Ladam G, Benkirane-Jessel N. Osteogenetic Properties of Electrospun Nanofibrous PCL Scaffolds Equipped With Chitosan-Based Nanoreservoirs of Growth Factors. *Macromol Biosci* 2014;**14**:45–55.

58. Simmons CA, Alsberg E, Hsiong S, Kim WJ, Mooney DJ. Dual growth factor delivery and controlled scaffold degradation enhance in vivo bone formation by transplanted bone marrow stromal cells. *Bone* 2004;**35**:562–9.

59. Park K-H, Kim H, Moon S, Na K. Bone morphogenic protein-2 (BMP-2) loaded nanoparticles mixed with human mesenchymal stem cell in fibrin hydrogel for bone tissue engineering. *J Biosci Bioeng* 2009;**108**:530–7.

60. Wang Z, Wang K, Lu X, Li M, Liu H, Xie C, Meng F, Jiang O, Li C, Zhi W. BMP-2 encapsulated polysaccharide nanoparticle modified biphasic calcium phosphate scaffolds for bone tissue regeneration. *J Biomed Mater Res A* 2015;**103**:1520–32.

61. Deng C, Zhang P, Vulesevic B, Kuraitis D, Li F, Yang AF, Griffith M, Ruel M, Suuronen EJ. A collagen–chitosan hydrogel for endothelial differentiation and angiogenesis. *Tissue Eng Part A* 2010;**16**:3099–109.

62. Ellis CE, Korbutt GS. 4 - Chitosan-based biomaterials for treatment of diabetes. In: Jennings JA, Bumgardner JD (eds.). *Chitosan Based Biomaterials Volume 2*. Woodhead Publishing, 2017, 91–113.

63. McBane JE, Vulesevic B, Padavan DT, McEwan KA, Korbutt GS, Suuronen EJ. Evaluation of a Collagen-Chitosan Hydrogel for Potential Use as a Pro-Angiogenic Site for Islet Transplantation. *PLOS ONE* 2013;**8**:e77538.

64. Farokhi M, Mottaghitalab F, Shokrgozar MA, Ou K-L, Mao C, Hosseinkhani H. Importance of dual delivery systems for bone tissue engineering. *J Controlled Release* 2016;**225**:152–69.

Appendix A Chitosan Scaffold Fabrication

A.1 Chitosan Scaffold Mechanical Properties

Chitosan scaffolds with varying wt% of chitosan were prepared in order to optimize the fabrication of scaffolds to be used in the proposed system. The rheometry data shown in **Figure A.1** suggests that an increase in wt% of chitosan has a slight effect on the storage and loss moduli of the materials, increasing from 6900 to 9100 Pa and decreasing from 628 to 551 Pa, respectively. However, an increase in chitosan wt% results in a noticeable increase in the viscosity of the chitosan solution. Because the scaffold fabrication process requires the casting of chitosan solution into molds, increased viscosity can results in a loss of material and the introduction of large air bubbles. It was therefore found that a 2 wt% formulation provided the best trade-off between higher mechanical properties and ease of handling.

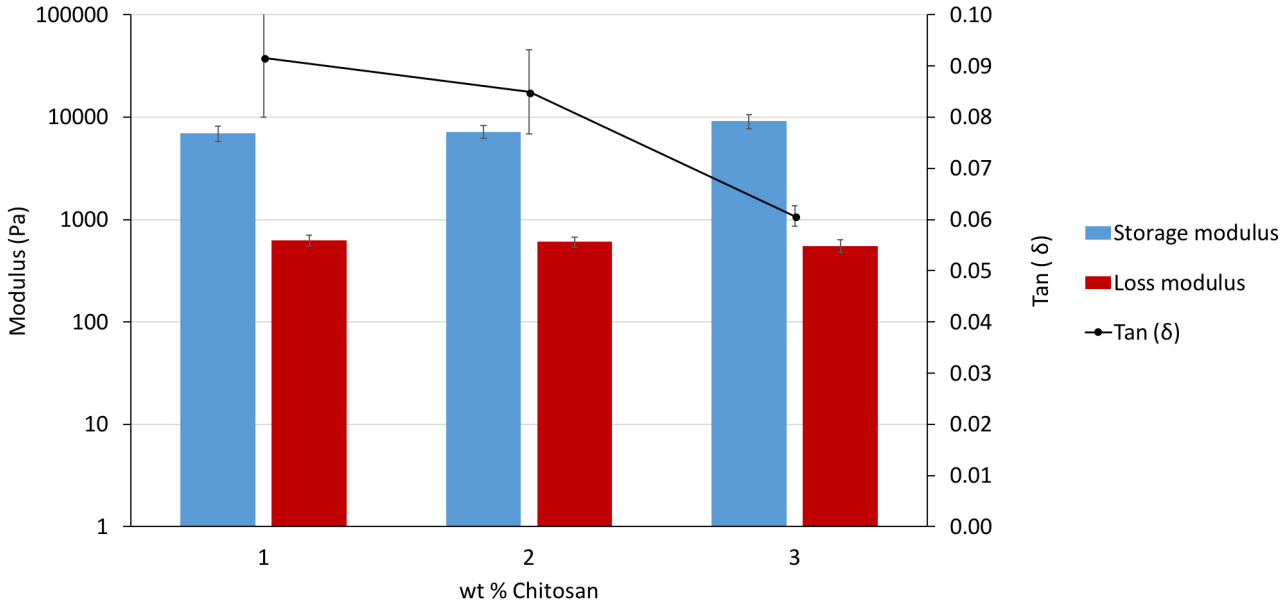

Figure A.1 - Dynamic mechanical properties of chitosan scaffolds with increasing wt% chitosan formulation

A.2 Scaffold SEM Imaging

In order to optimize chitosan scaffold formulations, the use of a chemical crosslinker was explored in order to determine the effect on scaffold mechanical properties and porous structure. Scaffolds with 0, 25, 50, and 75 mol% glutaraldehyde were prepared. Rheometer data indicated no significant effect of crosslinker incorporation on scaffold mechanical properties. Scanning electron microscope images further indicated that the incorporation of crosslinker does not significantly affect the pore structure within the scaffold bulk, as shown in **Figure A.2**. However, and effect of increased chitosan wt% on pore structure was observed, with increased wt% of chitosan resulting in a reduction in pore size.

Ultimately, the range in pore sizes observed for the 2 wt% chitosan scaffolds further informed the selection of this formulation for further use in the proposed system.

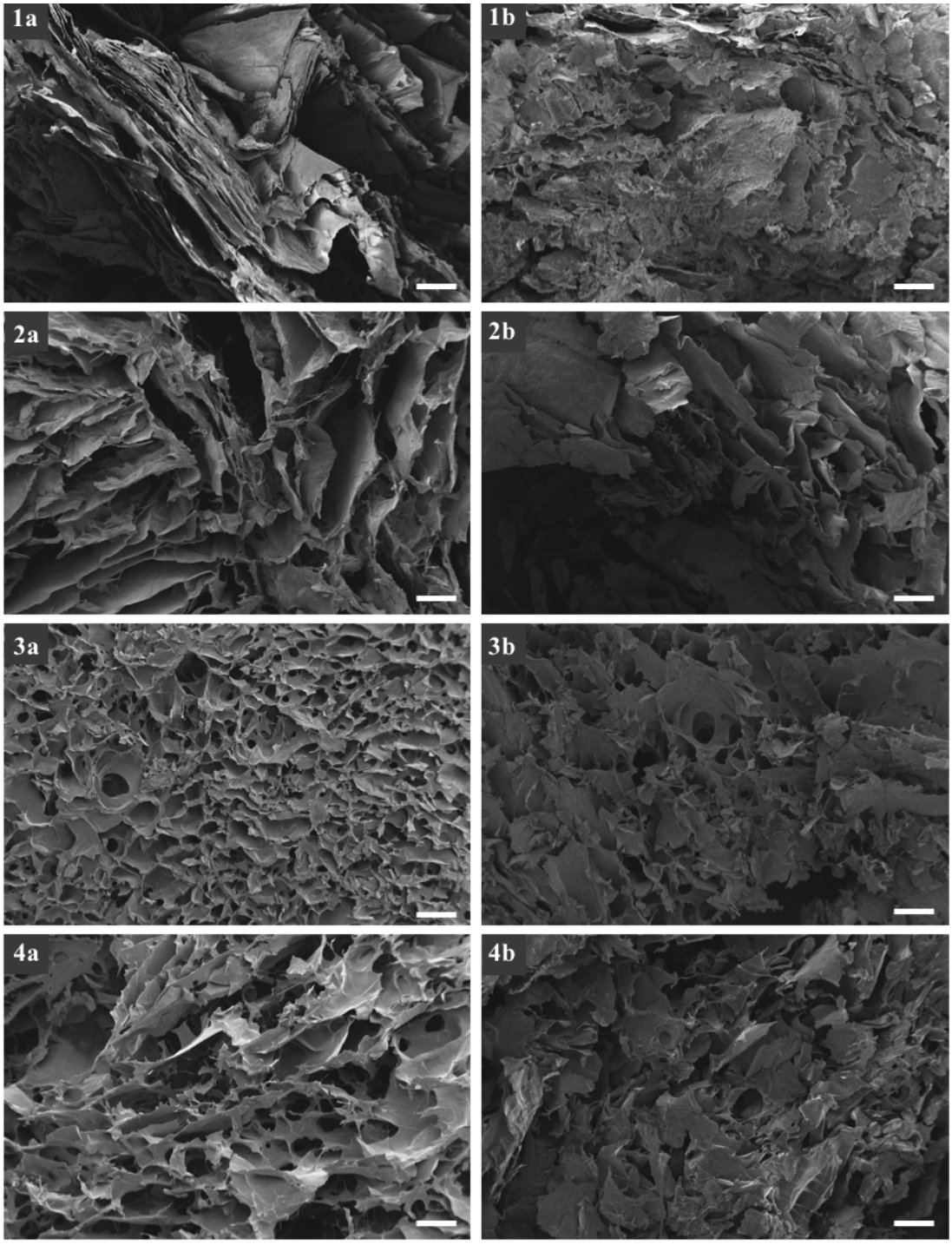

Figure A.2 - SEM images of 1 wt% (1), 2 wt% (2), 3 wt% (3), and 4 wt% (4) chitosan scaffolds without crosslinker (a) and with 25 mol% glutaraldehyde crosslinker (b). 100 x magnification, scale bars 300 μm

Appendix B Nanoparticle Fabrication

B.1 Reversible Aggregation

The reversible aggregation of P(MMA-co-MAA) nanoparticles is illustrated in **Figure B.1**. This phenomenon informs the chosen purification method, which relies on the formation of a particle pellet in an acidic solution and the resuspension of these particles in a buffer at pH ~ 7.

(1)

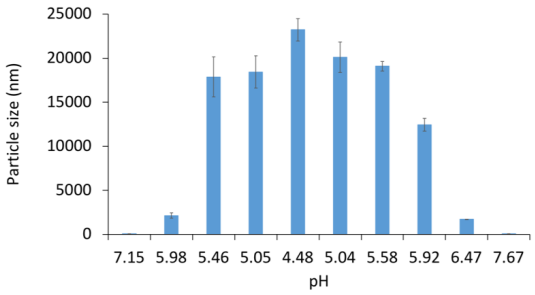

(2)

Sample	Average diameter (nm)	PDI
pH 7 - Initial	61.86	0.164
pH 7 – After aggregation	74.46	0. 143

(3)

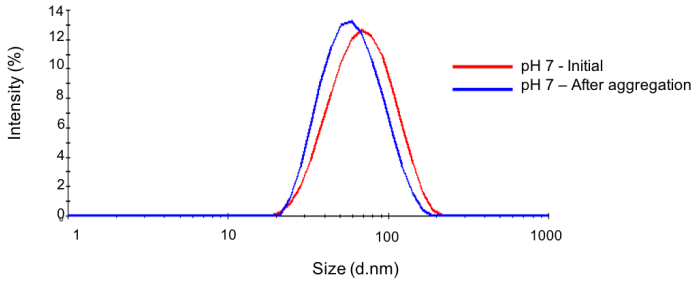

Figure B.1 - (1) Plot of recorded particle size in nm as a function of pH where pH is decreased from above pH 7 to pH 4.5 then increased again to above pH 7, (2) Average diameter and PDI of nanoparticles before and after reversible aggregation, (3) Intensity plots of the particle size for particles before and after reversible aggregation

Appendix C Protein Binding Study

C.1 Design of Experiments – JMP

The statistical software JMP was used in order to determine an experimental design which would allow for the development of a robust model for protein loading ability while minimizing the number of experimental runs required to achieve statistical power. Additional points of comparison between the 3x3x3x3 Factorial design and candidate designs are shown in **Figure C.1** and **Figure C.2**.

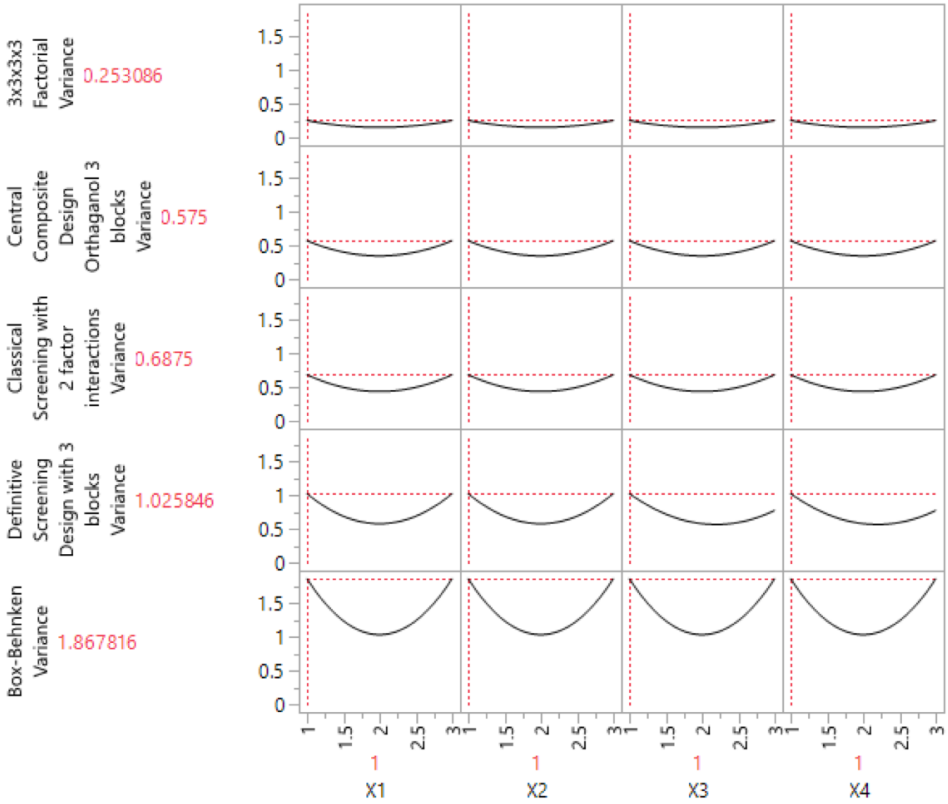

Figure C.1 - Prediction variance profiles for candidate experimental designs when compared to the 3x3x3x3 Factorial design

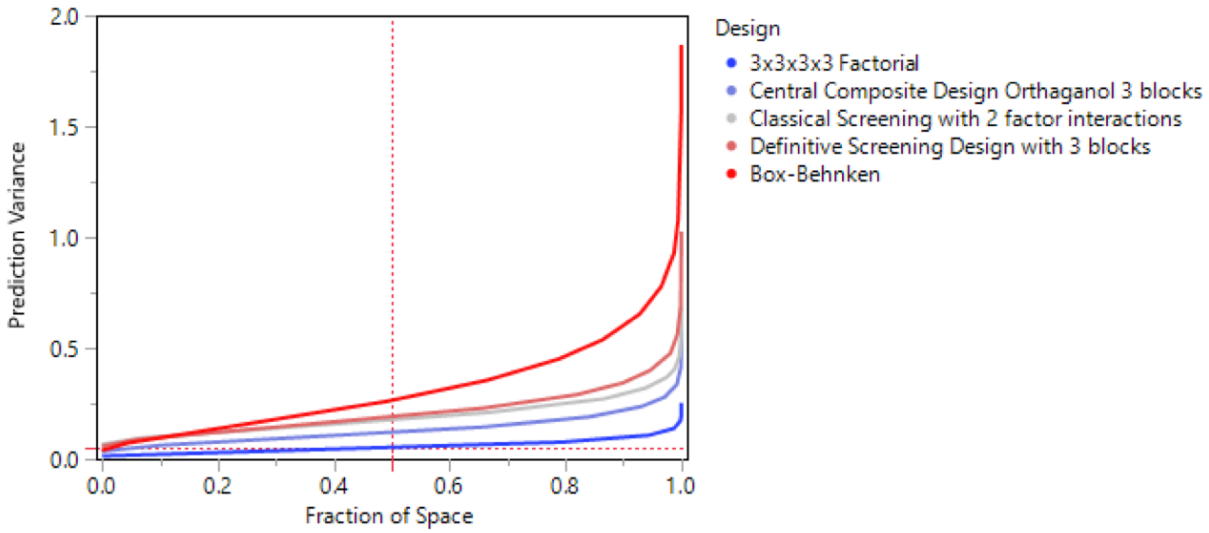

Figure C.2 - Fraction of design space having a given prediction variance for candidate experimental designs when compared to the 3x3x3x3 Factorial design

C.2 Description of Runs

Having selected the Classical Screening with 2-factor interactions experimental design, JMP defined the 23 distinct runs required in order to develop a predictive model for protein loading into nanoparticles. The patterns are defined by a combination of "+", "-" or "0" which correspond to either the lowest, highest or middle value tested for each loading condition, respectively. For example, Run 1 requires a "-+-+" pattern, which corresponds to the lowest loading time (2h), the highest pH (7.5), the lowest ionic strength (5 mM) and the highest protein to polymer ratio (10 wt%). A description of all experimental runs is shown in **Table C.1**.

Table C.1 - Description of experimental runs required for the Classical Screening experimental design as defined by JMP

Run	Pattern	Time (hr)	pH	Ionic Strength (mM)	Protein:Polymer (wt%)
1	−+−+	2	7.5	5	10
2	−−++	2	4.5	154	10
3	−++−	2	7.5	154	3
4	−−−−	2	4.5	5	3
5	−+−−	2	7.5	5	3
6	−−+−	2	4.5	154	3
7	−−−+	2	4.5	5	10
8	−+++	2	7.5	154	10
9	0A00	24	7.5	79.5	6.5

10	00A0	24	6	154	6.5
11	000A	24	6	79.5	13.5
12	0a00	24	4.5	79.5	6.5
13	0	24	6	79.5	6.5
14	00a0	24	6	5	6.5
15	+−−+	48	4.5	5	10
16	++++	48	7.5	154	10
17	+−++	48	4.5	154	10
18	+++−	48	7.5	154	3
19	++−+	48	7.5	5	10
20	++−−	48	7.5	5	3
21	+−−−	48	4.5	5	3
22	+−+−	48	4.5	154	3
23	A000	72	6	79.5	6.5

C.3 Predictive Model for Protein Loading Efficiency as a Function of Loading Variables

After analyzing the protein loading efficiency for the different runs the loading data was provided to the JMP software. The software then output a model which predicts the protein loading efficiency as a function of the four evaluated variables and provides the conditions at which loading is maximized. The 2-factor interaction profiles between the different variables are shown in **Figure C.3**.

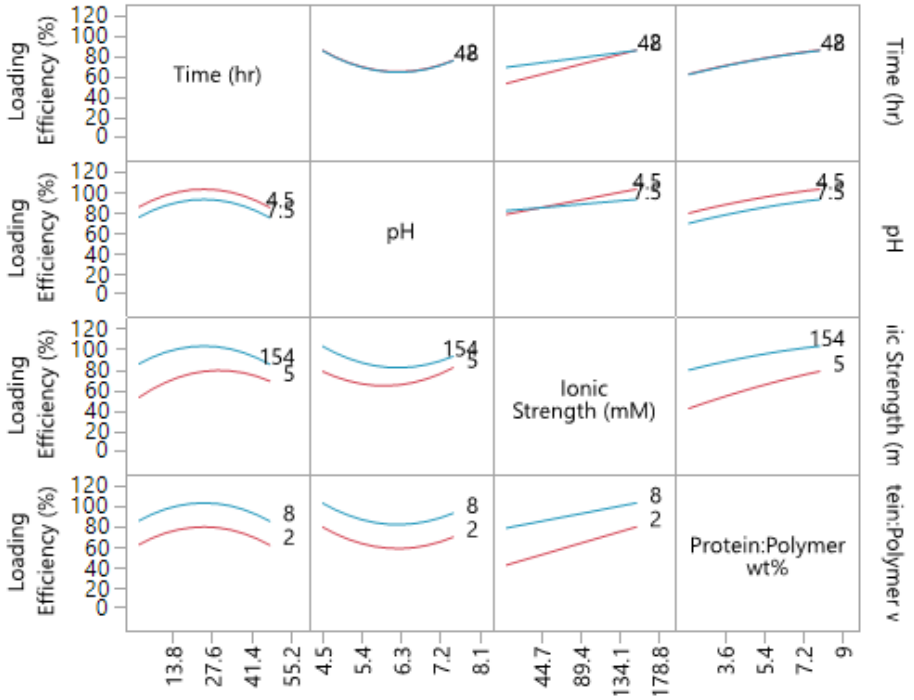

Figure C.3 - Interaction profiles between different loading condition variables

Appendix D Custom Crosslinker Synthesis

D.1 PLA-b-PEG-b-PLA Intermediate Characterization

In the two-step synthesis of the degradable MA-PLA-b-PEG-b-PLA-MA crosslinker, the successful incorporation of lactic acid units along the PEG chain was first verified by analysis of the intermediate product via 1-H NMR. The spectra of the intermediate products were compared to the spectrum of the initial PEG chain. As observed in **Figure D.1** the appearance of peaks at 5.2 ppm, 4.25 ppm, and 1.5 ppm are indicative of the presence of the lactic acid units.

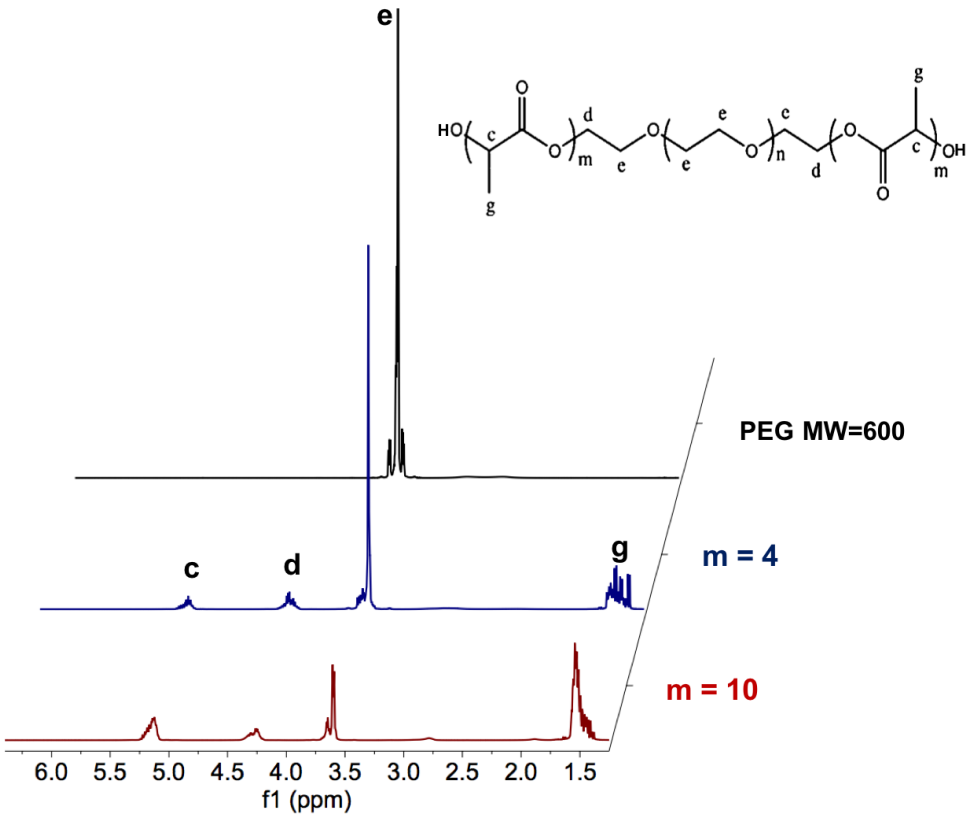

Figure D.1 - Comparison of the 1-H NMR spectra of poly(ethylene glycol) MW 600 (black) and the intermediate products of the ring opening polymerization reaction for increased number of lactic acid units incorporated (m=4 in red and m=10 in blue)

D.2 Custom Crosslinker Characterization – FTIR

In addition to NMR, the final custom crosslinker was characterized by FTIR. As can be seen from the spectra in **Figure D.2**, the comparison of the FTIR spectra for the custom crosslinkers to that of the reference PEGDMA shows distinct peaks indicative of the successful lactic acid incorporation and methacrylation of the custom crosslinkers. In particular, the appearance of peaks at 1800 cm^{-1} and 1250 cm^{-1} in addition to the appearance of a peak at 1750 cm^{-1} are indicative of the incorporation of lactic acid units and the successful methacrylation of the crosslinker, respectively.

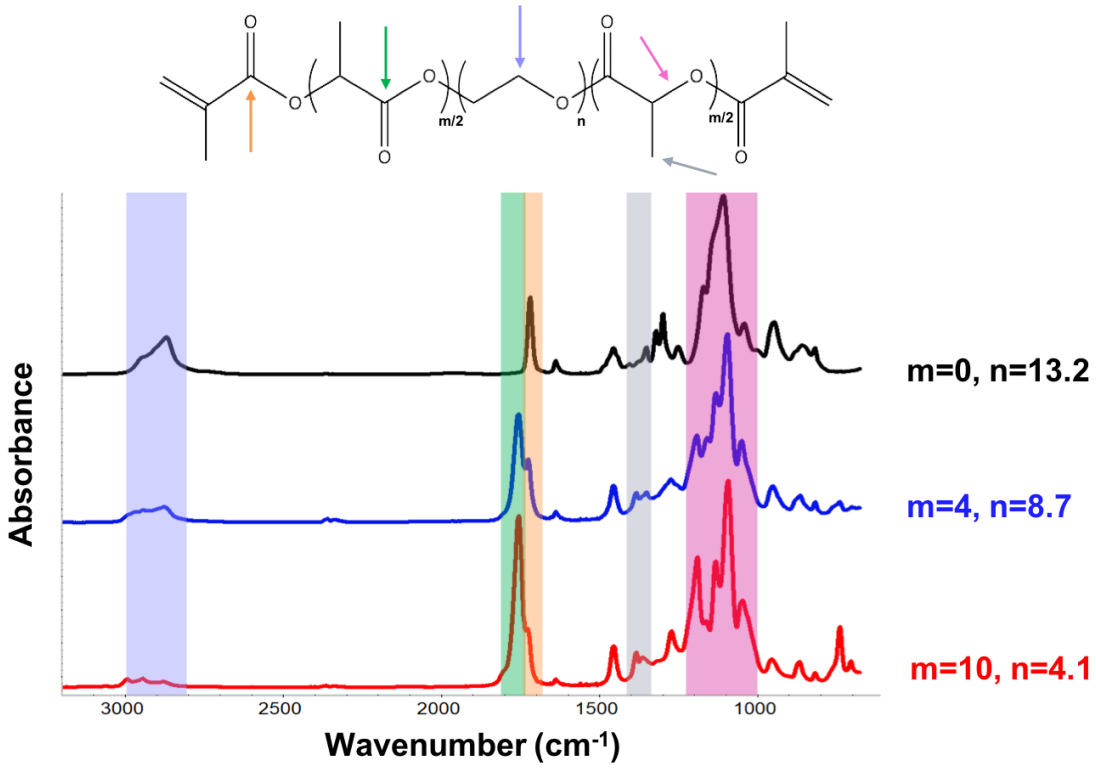

Figure D.2 - FTIR spectra for the crosslinkers used in the fabrication of nanoparticles with increasing degrees of degradability

Appendix E Nanoparticle Degradation

E.1 NMR Spectra of Nanoparticles for Kinetic Analysis

The 1-H NMR spectra for m = 0, m = 4, and m = 10 nanoparticles subjected to accelerated degradation conditions were obtained at various time points and plotted in **Figure E.1**, **Figure E.2**, and **Figure E.3**. Integration of the peaks at 1.18 ppm over time provided the degradation data included in **Figure 3.10**.

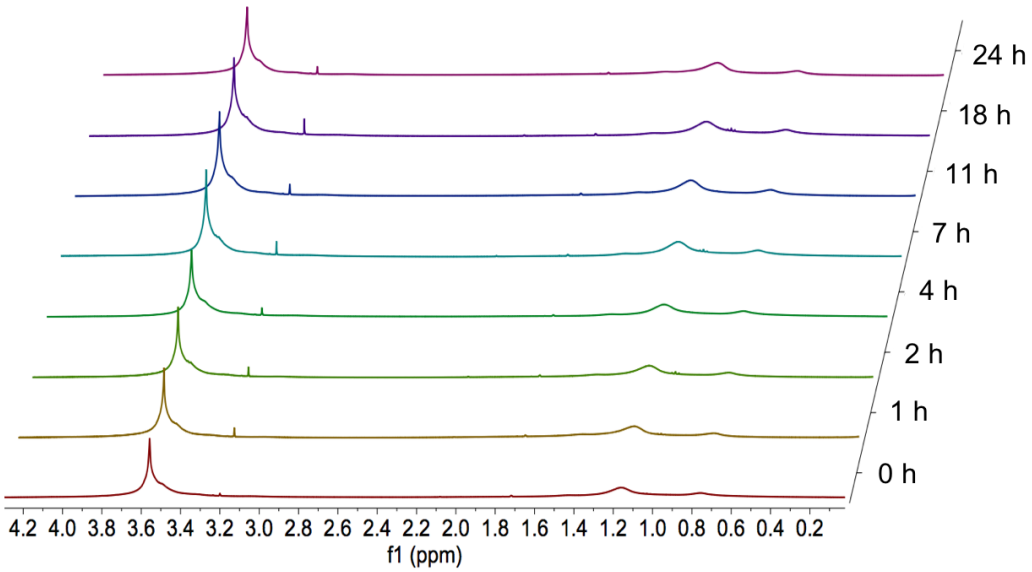

Figure E.1 - NMR spectra as a function of time for m = 0 nanoparticles subjected to accelerated degradation conditions in D_2O

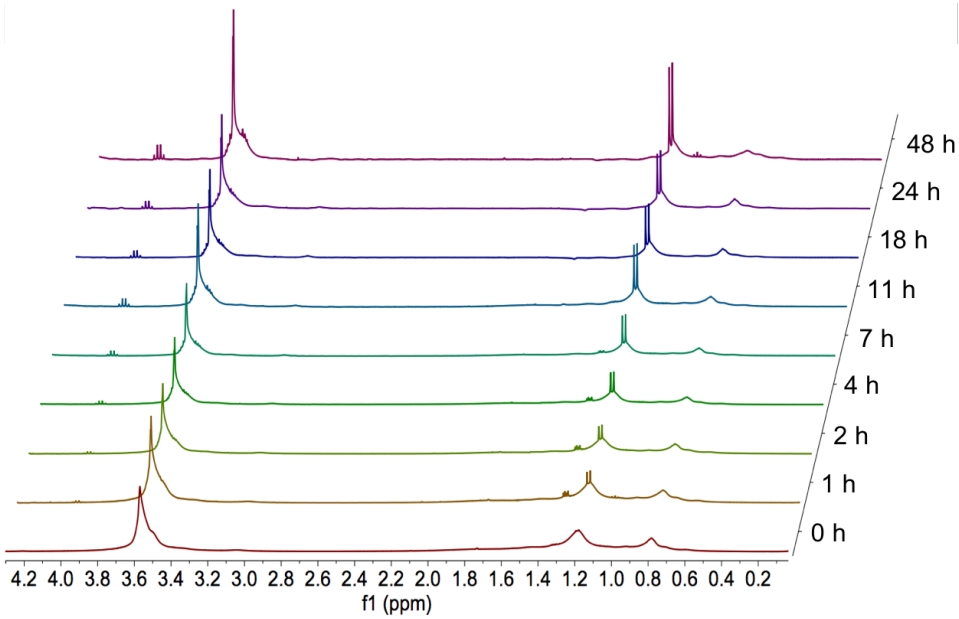

Figure E.2 - NMR spectra as a function of time for m = 4 nanoparticles subjected to accelerated degradation conditions in D_2O

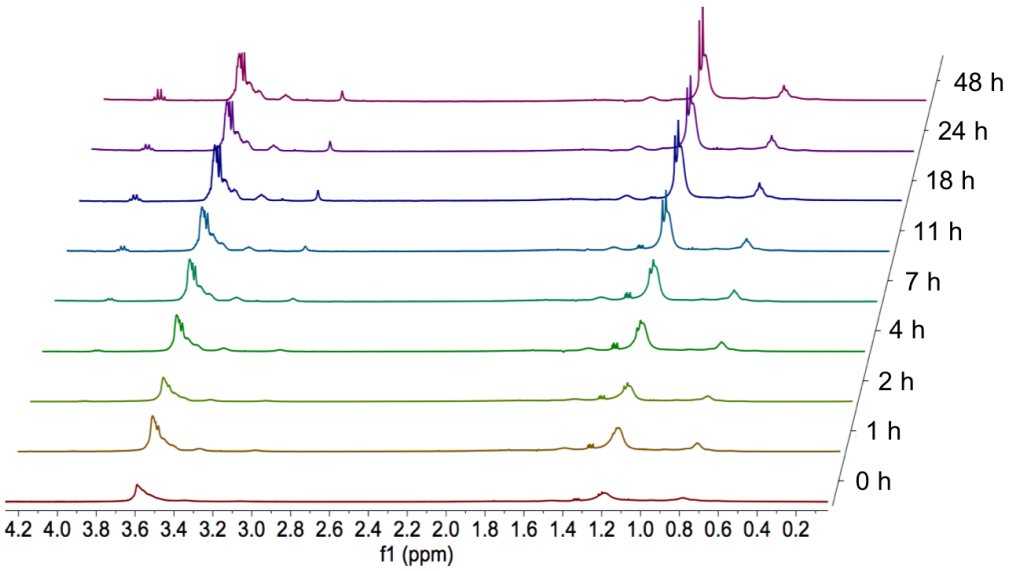

Figure E.3 - NMR spectra as a function of time for m = 10 nanoparticles subjected to accelerated degradation conditions in D_2O

Appendix F Covalent Binding of Nanoparticles to Scaffold Backbone

F.1 Fluorescent labelling experiment.

Washes were performed every 5 minutes for the first 30 minutes, after 24, 72, and 4 weeks on scaffolds containing fluorescently labelled protein and nanoparticles. After each wash, the supernatants were plated on a 96 well plate. For the DAPI-labelled protein, fluorescence was analyzed at an excitation wavelength of 358 nm and an emission wavelength of 461. For the tamra cadaverine-labelled nanoparticles, fluorescence was analyzed at and excitation wavelength of 552 nm and an emission wavelength of 578. The obtained fluorescence values were fitted to calibration curves for the labelled components in order to obtain values of the concentration of fluorescently labelled components in the supernatant. The cumulative release as a function of time was then plotted (**Figure F.1**).

A rapid burst release was observed for the adsorbed protein and nanoparticles, with over 60% released within the first 5 minutes for both systems and 100% release after 4 weeks. An initial burst release of about 3% within the first 5 minutes was observed for the covalently bound nanoparticles with no further release for up to 4 weeks. This result further confirms that the covalent binding of nanoparticles to the scaffold backbone allows for their sustained retention within the scaffold over time.

The initial burst release observed for the bound nanoparticles can be explained by the diffusion of any particles not successfully bound to the scaffold backbone during the EDC-NHS reaction. The release profiles observed for the non-bound protein and nanoparticles show a more rapid release of the nanoparticles from the scaffold and can be explained by their larger size when compared to the protein. Indeed, the protein being smaller than the nanoparticles relative to the scaffold pores allows them to diffuse along more paths through the scaffold pore network and may therefore delay their clearance out of the scaffold bulk and into the surrounding fluid.

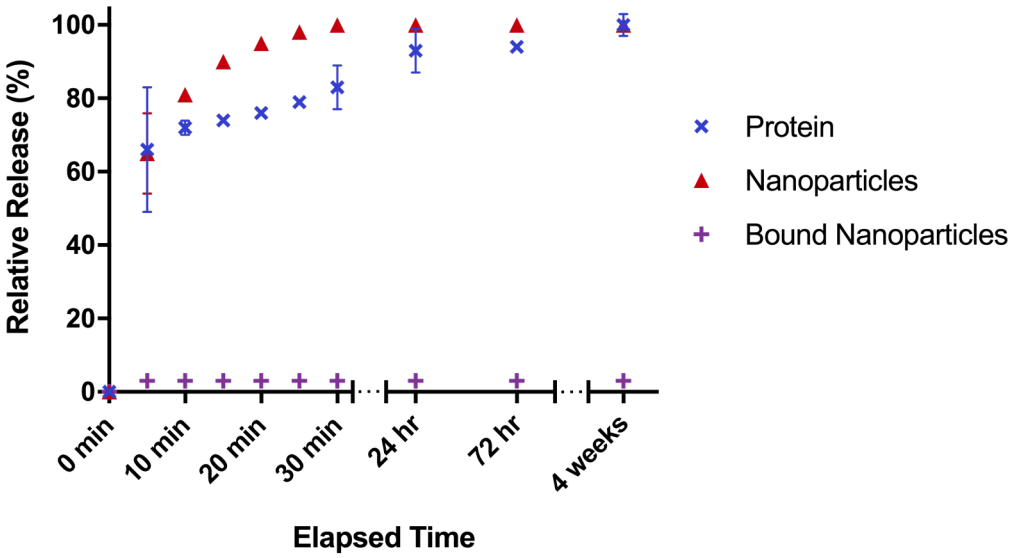

Figure F.1 - Relative cumulative release of DAPI-labelled protein (blue), tamra cadaverine labelled nanoparticles (red), and tamra cadaverine labelled bound nanoparticles (purple) from a chitosan scaffold as a function of time

Appendix G In Vitro Cytotoxicity Experiments

G.1 MTS Cellular Proliferation Assay

A summary of the MTS cellular proliferation assay results shown in **Figure 3.17.A** and **Figure 3.18.A** is provided in **Figure G.1**.

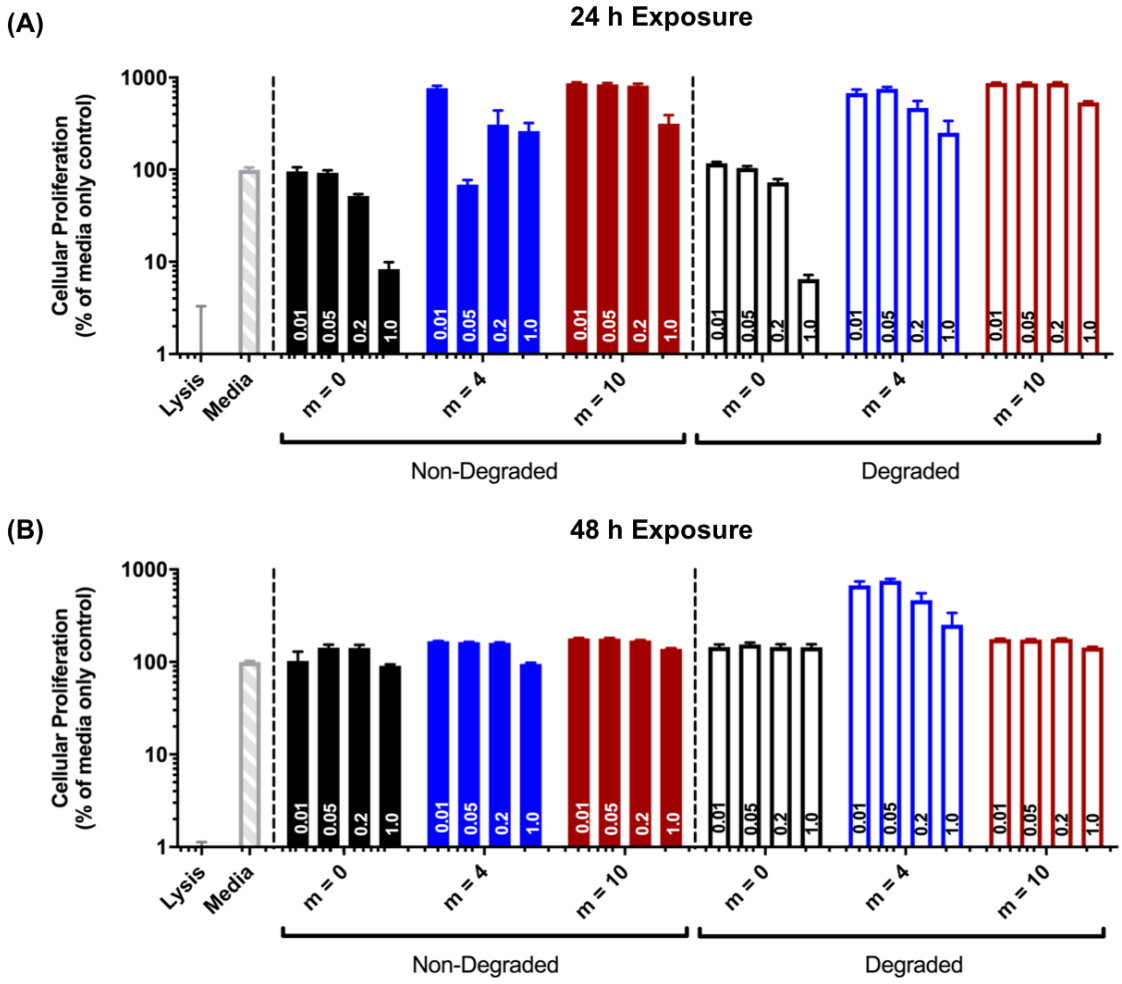

Figure G.1 - Summary of MTS cellular proliferation assay evaluating the compatibility of degradable P(MMA-co-MAA) nanoparticles with HUVECs when compared to the media and lysis controls after (A) 24 h exposure and (B) 48 h exposure

G.2 LDH Cell Viability Assay

A summary of the MTS cellular proliferation assay results shown in **Figure 3.17**.**B** and **Figure 3.18**.**B** is provided in **Figure G.2**.

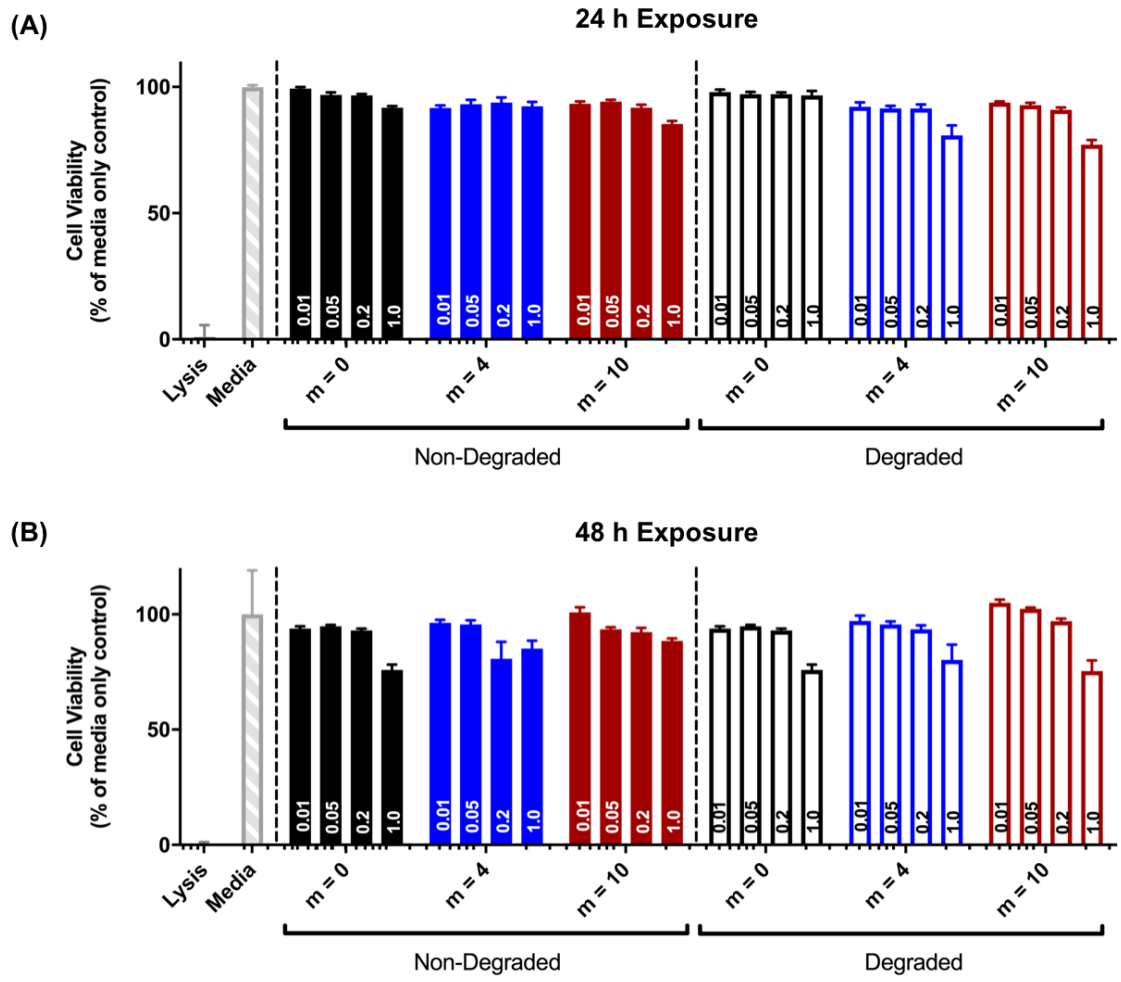

Figure G.2 - Summary of LDH cell membrane integrity assay evaluating the compatibility of degradable P(MMA-co-MAA) nanoparticles with HUVECs when compared to the media and lysis controls after (A) 24 h exposure and (B) 48 h exposure